LOW-ENERGY GAMMA RAYS IN THE ATMOSPHERE

Jerome S. Puskin

CHAPTER I

INTRODUCTION

With the advent of high-altitude balloons, rockets and satellites, it has been possible to extend astronomical observations into regions of the electromagnetic spectrum for which the Earth's atmosphere is opaque. Besides supplementary infrared, ultraviolet and radio work, these advances have given rise to the fields of x-ray and gamma ray astronomy. We shall focus, primarily,on the low energy gamma ray region (.3-10 Mev).

Before turning to the major concern of this thesis, the atmospheric background flux that makes measurements in this region very difficult, let us review briefly the interest in such investigations. Gamma rays are believed to be created throughout the Universe by the interaction of high energy particles with ambient radiation, matter and fields, according to the same physical laws everywhere. Because these quanta travel in straight lines and are highly penetrating, determination of their arrival directions, energy spectrum, and intensity can provide important information on particle fluxes, energy and matter densities, the strength of magnetic fields, and nuclear processes present in objects of astrophysical interest and in galactic and metagalactic space.

This work was supported in part by Contract F 19628-68-C-0297 from the United States Air Force.

The chief production mechanisms of low energy gamma rays are:

(a) Electron bremstrahlung: the inelastic scattering of electrons from the coulomb field surrounding a nucleus or another electron.

(b) Synchrotron radiation (magnetic bremstrahlung), the emission of radiation by a relativistic electron in the presence of a magnetic field component perpendicular to the particle momentum - the power radiated is inversely proportional to the fourth power of the mass while the typical frequency of emission is inversely proportional to the cube of the mass, for fixed momentum; therefore, gamma ray synchrotron emission by protons and heavier particles is entirely negligible.

(c) Inverse Compton scattering, the scattering of electrons from photons with energy transfer from the former to the latter.

(d) Positron annihilation.

(e) Nuclear de-excitation.

(f) π^o-decay.

These processes can only occur as the result of electron acceleration or as a consequence of secondary particle production in high energy strong interactions. This immediately suggests that we can learn something about the origin and

traversal of cosmic rays in the Galaxy and the metagalaxy. The power of gamma ray astronomy here is that the gamma rays travel in straight lines while the cosmic rays themselves are deflected by Galactic magnetic fields and arrive at the Earth practically isotropic (except for the East-West asymmetry caused by the terrestrial field). There exist many reviews discussing the utilization of gamma ray measurements, in conjunction with cosmic ray and radio data, to determine the density and composition of matter, the time history of high energy particles, the photon energy density and spectrum in the Galaxy and in intergalactic space (Gould and Burbidge 1965; Ginzburg and Syrovatskii 1964 a,b; Fazio 1967; Greisen 1968).

Observation on the diffuse flux in the 60 kev to one Mev energy range have been made on two flights of Ranger moon probes (Arnold, et al. 1962; Metzger at al. 1964). The intensity they detected (See Chapter V) is too high to be accounted for by the processes listed above operating in the present observable Universe. Consequently, it appears that these photons were produced in the distant past and are of great cosmological significance, (Greisen 1968). Detailed directional studies are necessary to separate out the Galactic component of the radiation.

Although the acceleration mechanism is not well understood, supernova (SN) explosions appear to be the predominant

energy source for the acceleration of high energy particles (Ginzburg and Syrovatskii 1964a). Photons with energy up to 560 kev, apparently of synchrotron origin, have been discovered to be arriving from Crab Nebula, a SN remnant (Haymes, et al. 1968). This requires the continual acceleration of electrons to 2×10^{14} ev.

SN explosions are also believed to be of central importance in the synthesis of the elements. These stars reach the silicon burning stage, at least; and following the explosion, the nuclear debris is blown out into interstellar space where it can condense into new stars (Burbidge, Burbidge, Fowler and Hoyle, 1957).

Further study of the X-ray and gamma ray continuum radiation will shed light on the acceleration mechanisms. This research is particularly interesting since the discovery of the pulsar in the Crab. In fact, the X-ray intensity pulsates at the same frequency as the radio and optical radiation (Fritz et al. 1969; Bradt et al. 1969; Fishman et al. 1969). Detection of nuclear line radiation emitted from a SN would aid in the understanding of the nuclei acceleration mechanisms, the dynamics of the explosion and nucleosynthesis. Predictions of nuclear de-excitation line intensities have been made from various SN models (Savedoff, 1959; Clayton and Craddock, 1965; Clayton, Colgate, and Fishman, 1969).

Recently, it has been suggested that a smeared out quasi-continuum of such radiation may exist from the superposition of many redshifted metagalactic sources (Clayton and Silk, 1969). Confirmation would make possible an analysis of the history of element synthesis in the Universe.

Sartori and Morrison (1967) have argued from very general considerations that synchrotron radio sources such as Q.S.O.'s, radio galaxies and SN remnants are potential x-ray and gamma ray emitters. The crux of the argument is that any acceleration mechanism, e.g., a shock wave, must be inefficient to some degree and energy will be transferred to the ambient gas. If this energy is not radiated fast enough, the gaseous medium will heat up as long as the acceleration process continues. Sartori and Morrison show that it is quite reasonable to expect heating up to the point where kT is thousands or even millions of electron volts.

During solar flare activity, the Sun emits energetic particles. The acceleration mechanisms may be qualitatively much like those for cosmic rays. If this turns out to be the case, the Sun's proximity may allow observations that will facilitate the solution of the problem of cosmic ray origin; this, despite the fact that objects like the Sun contribute very little to the Galactic proton flux and only then

at rather low energies ($E \lesssim 1$ Bev). Gamma rays are generated in a flare by bremstrahlung; by positron annihilation - the positrons, in this case, are produced chiefly by nuclear proton decay; and by nuclear de-excitation (Dolan and Fazio 1965, Kuzhevskii 1969).

While the first of these results from the acceleration of electrons, the latter two imply proton acceleration. A time profile of the gamma ray spectrum before, during and after a flare would elucidate the acceleration process. Interesting questions to be answered are:

1. Are the particles accelerated prior to or following the optical flare?
2. Are separate mechanisms operative for electron and heavy particle acceleration?
3. Where are the particles accelerated and stored?
4. Are flares really different in kind, or only in intensity?

Finally, it has been hypothesized that element transmutation in flares of the early protosun significantly modified the chemical composition of the solar system (Fowler, Greenstein and Hoyle 1962). In order to test this theory, more has to be known about the nuclear reactions occurring in flares. The gamma ray line spectrum from a flare would be particularly helpful.

In spite of the plethora of interesting potential sources to look at, there is a scarcity of positive results. The difficulties are the relatively low number of photons arriving from these sources and the high intensity of background radiation produced in the atmosphere and the surrounding material. In the low energy gamma ray region, especially above 1 Mev, it is very hard to build an effective shield against penetrating background. The problem is accentuated by the need to limit the weight of balloon or satellite payloads. In order to design an optimum low energy gamma ray instrument for balloon borne observations, it is necessary to know the intensity, energy spectrum, and angular distribution of the background gamma radiation in the atmosphere. It is hoped that the following will be a step forward in that endeavor.

CHAPTER II

THE LOW ENERGY GAMMA RAY FLUX AT BALLOON ALTITUDE

Incident cosmic rays interact with atmospheric atoms to generate a large number of secondary particles; these secondaries, along with re-entrant albedo electrons (primary electrons are negligible in comparison), produce gamma rays by the mechanisms listed in the introduction. These gamma rays subsequently move through the atmosphere, often degraded and deflected by scattering from atomic electrons, before escaping or being absorbed. In this chapter we shall calculate the low energy gamma ray flux at balloon altitude and medium latitude, which we take to be 3.5 g/cm^2 residual pressure and 41^o, respectively.

The gamma ray spectrum at altitude p^*, energy E^*, direction Ω^*, can be represented by:

$$j(E^*,p^*,\Omega^*)=\int S(E,p,\Omega)G(E^*,p^*,\Omega^*;E,p,\Omega)dEdpd\Omega \qquad (1)$$

where $S(E,p,\Omega)$ is the source function for the number of photons ($cm^{-2}sec^{-1}Mev^{-1}sr^{-1}mb^{-1}$) of energy E and direction Ω produced at depth p, and $G(E^*, p^*,\Omega^*; E,p,\Omega)$ is the probability that a photon produced with energy E at depth p with direction will arrive at p^* with energy E^* and direction Ω^*. G is, of course, independent of S; consequently we can separate the problem into three parts:

(a) Determination of G the transmission function.

(b) Determination of S the source function.

(c) Substitution of (a) and (b) into (1) in order to calculate j.

(A) Gamma Ray Transmission in the Atmosphere

A gamma ray, in traversing the atmosphere, can interact with the gas atoms through:

(a) Compton scattering - the gamma ray can scatter elastically from an atomic electron and emerge with reduced energy and altered direction.

(b) Pair production - the gamma ray can materialize into an electron-positron pair in the presence of a Coulomb field about a nucleus or electron.

(c) Photoelectric absorption - a gamma ray can be totally absorbed by an atom with an electron being ejected.

For our purposes, i.e., photon energies in excess of 300 kev, we can neglect photo-electric absorption in the atmosphere. Some representative cross-sections for Compton scattering and pair production are displayed in Table 1 and 2, respectively. These cross-sections are easily converted to the more convenient unit, cm^2/g; then absorption lengths can be expressed in g/cm^2, the same unit we use for depth.

In order to trace the history of simulated gamma rays through the atmosphere, we have developed a Monte Carlo

Table 1

Compton Cross-Sections
(Bethe and Ashkin 1953)

$E_\gamma / m_e c^2$	$\sigma_{Compton}$ (10^{-25} cm^2/ electron)
.50	3.744
1.0	2.866
2.0	2.090
3.0	1.696
4.0	1.446
6.0	1.136
8.0	.9465
10.0	.8168
70.0	.1911
200.0	.08118

Table 2

Pair Cross-Sections
(Davisson 1965)

E Mev	Oxygen Barns/atom	Nitrogen Barns/atom
2	.0086	.011
4	.041	.055
8	.092	.119
50	.260	.333
100	.319	.408

program, ATMSCAT. ATMSCAT takes a photon initialized with energy E, zenith angle α, at depth Pi, and sequentially (a) allows the photon to interact at Pf where (see appendix)

$$\gamma = e^{-(P_f - P_i)\,\sigma_\tau/\cos\alpha} \tag{2a}$$

or,

$$Pf = Pi + (\log \gamma)\,\cos\alpha/\sigma_\tau \tag{2b}$$

where γ is a random number selected uniformly between 0 and 1, $\sigma_\tau = \sigma pair + \sigma Compton$ in cm^2/g (Note: $\cos\alpha$ can be positive or negative, so Pf can be either greater than or less than Pi).

(b) checks to see if the photon has crossed the chosen balloon altitude (3.5 g/cm^2). If so, the event is scaled in the appropriate energy-angle bin.

(c) chooses the interaction at Pf to be either pair production or Compton scattering according to a random selection weighted by the respective cross-sections. If again, γ is a random number from a uniform distribution in the interval (0,1) and if

$$\gamma > \frac{\sigma\ Compton}{\sigma_\tau} \tag{3}$$

then the interaction is chosen to be pair production and the photon is considered lost. A photon that arises from bremstrahlung or annihilation of a pair produced lepton is already included under its proper source function. If, on the other hand, the opposite inequality holds, the interaction is taken

to be Compton scattering and subroutine finds Θ, the angle of scattering, by the Monte Carlo procedure weighted by the Klein-Nishina differential cross-section

$$\frac{d\sigma}{d\Omega} = \frac{r_o^2}{2}\left(\frac{E'}{E}\right)^2\left[\frac{E}{E'} + \frac{E'}{E} - \sin^2\Theta\right] \qquad (4)$$

where E is the incident energy, E' is the scattered photon energy and r_0 is the classical electron radius. E' can be eliminated from (4) by

$$E' = \frac{E}{1 + (1-\cos\Theta)E/mc^2} \qquad (5)$$

The value for Θ obtained in this way is easily combined with a randomly chosen azimuthal angle about the incident direction and the original zenith angle to yield the new zenith angle. The new energy is determined from (5).

(d) goes back to step (a), continuing to follow the photon until it is lost to space, earth, pair production, or energy degradation below 300 kev.

(B) Gamma Ray Production in the Atmosphere

We can break up S, the source function, into a sum over the independent processes for gamma ray production:

$$S(p,E,\Omega) = \sum_{i=1}^{N} S_i(p,E,\Omega) \qquad (6)$$

Not only will this simplify the calculation, but will provide insight into the relative contributions by the various processes.

1. Synchrotron Radiation

Relativistic electrons moving in a magnetic field emit photons about a characteristic frequency $\nu_c \approx 4.6 \times 10^{-6} B_\perp E^2$, where $B_\perp$ is the component of the magnetic field perpendicular to the electron velocity and E is the electron energy in ev (Ginzburg and Syrovatskii 1964a). At 400 kev quantum energy ($\nu = 10^{19}$ sec.$^{-1}$), and B $\simeq$ 1 gauss, E $\simeq$ 1.5 x 10^{12} ev. Electrons above this energy constitute a negligible fraction of the electron flux so this is not a significant source.

2. Inverse Compton Scattering

The average energy transferred to a photon in a collision with a high energy electron is

$$\overline{\Delta E} = k \left(\frac{E}{mc^2} \right)^2 \qquad (7)$$

where the energies of the incident electron and photon are E and k, respectively. The quanta emitted by the Sun are 1.4 ev, on the average, so that 1 Bev electrons can, in theory, scatter from these photons with the scattered quanta falling in the low energy gamma ray region. However, as pointed out by Dolan and Fazio (1965), an electron starting out from the Sun has about a 10% probability of Compton scattering before reaching the Earth. It is not hard to see, since the probability of scattering is proportional to photon density, that few cosmic ray electrons will scatter during their journey through the solar system. The generation of

gamma rays by inverse Compton scattering in the Earth's atmosphere is miniscule and entirely negligible compared to the production of bremstrahlung gamma rays by these same electrons.

3. Electron Bremstrahlung

Brini et al. (1967) estimated the X-ray production in the atmosphere at $\lambda = 45^{o}$ from electron bremstrahlung in conjunction with Compton scattering. They were mainly interested in the 40 kev to 200 kev portion of the spectrum. We shall adopt a similar approach in this section to the low energy gamma ray region, but with more precision in the representation of the electron spectrum, more accurate approximation to the bremstrahlung cross-section, and with the advantage of the Monte Carlo path-tracing routine.

In order to completely specify the source function for bremstrahlung, we need to know the entire energy spectrum, angular distribution, and intensity of electrons as a function of depth in the atmosphere. Further, it is necessary to have the differential cross-section in air for bremstrahlung $d\sigma/d\Omega dE_{\gamma}$ as a function of electron energy.

3a. The Electron Flux

Only the vertical and omnidirectional electron intensities have been measured in any detail. The angular distribution of electrons, as a function of atmospheric pressure is unknown. Let us temporarily make the assumption that

the bremstrahlung gamma rays are produced isotropically over each hemisphere, separately, and in proportion to the respective vertical electron intensity.

The vertical electron flux (upward and downward moving, separately) has been measured by Verma (1967) from 10 Mev to 1100 Mev as a function of depth in the atmosphere. The balloon flights were carried out at Palestine, Texas: $\lambda = 41^{o}$, 4.9 Bv geomagnetic cut-off. The data is summarized by Figures 1 and 2. An analytical approximation to those curves is

$$i_{down}(p) = 4.1 \times 10^{-2}\,cm^{-2}\,sec^{-1}\,sr^{-1} \quad 0<p<10mb \tag{8a}$$

$$i_{down}(p) = 6 \times 10^{-3} p^{.83}\,cm^{-2}\,sec^{-1}\,sr^{-1} \quad 10<p<100mb \tag{8b}$$

$$i_{up}(p) = 7 \times 10^{-2} e^{.01p}\,cm^{-2}\,sec^{-1}\,sr^{-1} \quad 0<p<60mb \tag{8c}$$

We can estimate the upward electron flux at greater depth. There is a peaking of energetic particle intensities at about 100 g/cm^2 (Pfotzer maximum): see, for example, Fig. 3. A reasonable choice is to extrapolate (8c) to p = 80mb and at $p \geq 80mb$ to set

$$i_{up}(p) = i_{up}(80) \quad 80<p<120mb \tag{8d}$$

We shall neglect gamma ray production by upward moving electrons for $p > 120$ g/cm^2. It was discovered in preliminary Monte Carlo runs that gamma rays produced upward at $p > 120mb$

1970SAOSR.318.....P

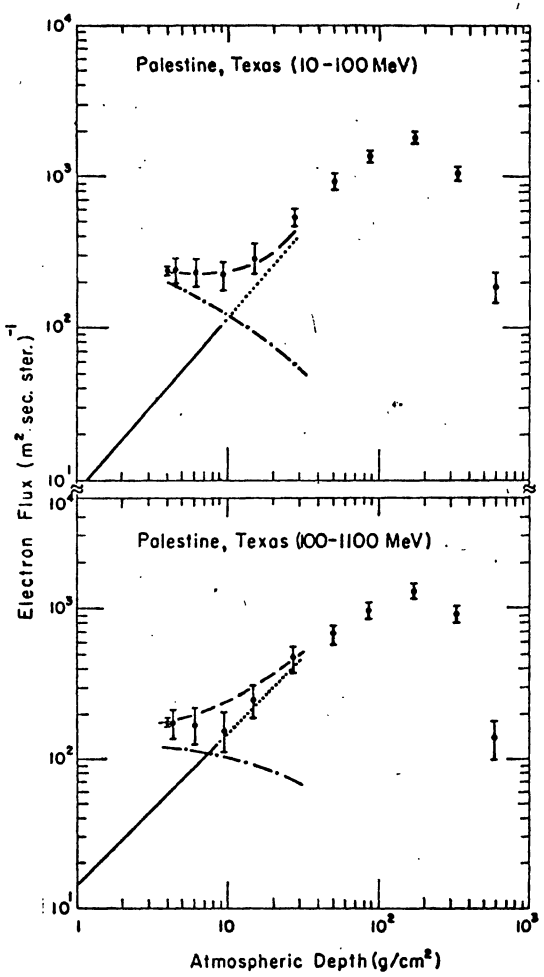

Figure 1. Downward Atmospheric Vertical Electron Intensity (Verma 1967).

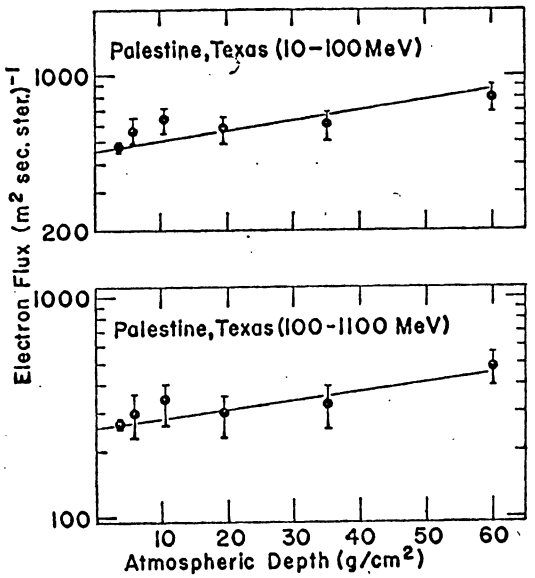

Figure 2. Upward Atmospheric Vertical Electron Intensity (Verma 1967).

or downward at P>30 mb make less than a 3% contribution to the low energy gamma ray flux at p = 3.5 mb. Moreover, it was found that the calculated flux at 3.5mb was insensitive to the precise choice for extrapolation when p>60 mb. These results are not surprising if one notes that the interaction length for gamma rays in air is never more than about 50 g/cm^2, and is typically 10-35 g/cm^2 in the low energy region.

Verma also measured the differential electron energy spectrum at p ≈ 4 g/cm^2. The splash upward albedo obeyed a power law

$$j(E) \sim E^{-1.3} \qquad 10 < E < 1100 \text{ Mev} \tag{9a}$$

while the downward flux at the top of the atmosphere was best described by

$$j(E) \sim E^{-1.44} \qquad 20 < E < 1250 \text{ Mev} \tag{9b}$$

Because of the cut-off below 4.9BV, these electrons too must have their origin in the atmosphere. They were splash albedo particles that were trapped by the Earth's magnetic field, reentering the atmosphere, perhaps many thousands of miles from their origin. Hence, the name reentrant albedo.

From the near equality of the slopes in the 10-100 Mev and the 100-1100 Mev curves (Fig. 1) for upward moving electrons, one is led to assume that (9a) is a good approximation

for the depth range of interest. In the absence of definitive measurements, we shall assume this to be the case. The bulk of downward produced bremstrahlung crossing p = 3.5mb is radiated in the top 10 grams of material. Consequently, no serious error is likely in adopting (9b) for all downward moving electrons.

The spectrum falls off more steeply above 1 Bev; the exponent in the power law is about 3, up to cut off. Primary electrons, in contrast to protons, are much less intense than the albedo. The probability of an electron of energy E_e radiating a photon of energy E_γ in the small interval ΔE_γ, ($E_\gamma << E_e$) is not strongly dependent on E_e. The conclusion is that electrons with energies above 4.5 Bev contribute a negligible fraction of the low energy gamma ray bremstrahlung.

At low energies the electron spectrum flattens. In the 3.3 - 4.5 Mev region at middle latitude ($\lambda \simeq 31\text{-}51^o$), the secondary electrons obey a power law with exponent between 1 and 1.2 (Charakhch'ian and Charakhch'ian 1959).

From the limited data available, we shall make the electron flux:

$$j(E) \sim E^{-1.05} \qquad E < 35 \text{ Mev} \qquad (10a)$$

for both upward and downward moving electrons,

$$j_{up}(E) \sim E^{-1.3} \qquad 35 < E < 1000 \text{ Mev} \qquad (10b)$$

$$j_{down}(E) \sim E^{-1.44} \qquad 35 < E < 1000 \text{ Mev} \qquad (10c)$$

and for both upward and downward moving electrons,

$$j(E) \sim E^{-3} \qquad 1 < E < 4.5 \text{ Bev} \qquad (10d)$$

The true electron energy spectrum will vary in shape to some extent with depth. However, the variation is not expected to be large for the cases of greatest interest: upward moving electrons in the top 60 or so grams of atmosphere, and downward moving electrons in the top 10 grams. The normilization of the electron flux is temporarily taken to be such that:

1. The expressions (10a-d) above are matched at the boundaries of definition.
2. The total flux between 10 Mev and 1100 Mev agrees with equations (8a-d) as a function of p. Below we shall be forced to revise this normalization.

Brini et al. (1967) have investigated the omnidirectional electron intensity above 1 Mev as a function of altitude. The fluxes,as displayed in Figure 3, should all be reduced by a factor of two, because Brini, et al. took the particle flux to be entirely downward and consequently, divided the number of counts per square centimeter per second by 2π rather than by 4π steradians to obtain the directional intensity (private communication).

If the electron flux were isotropic over each hemisphere, one would expect, because of the low energy threshold, a larger intensity per solid angle to be recorded on Brini's

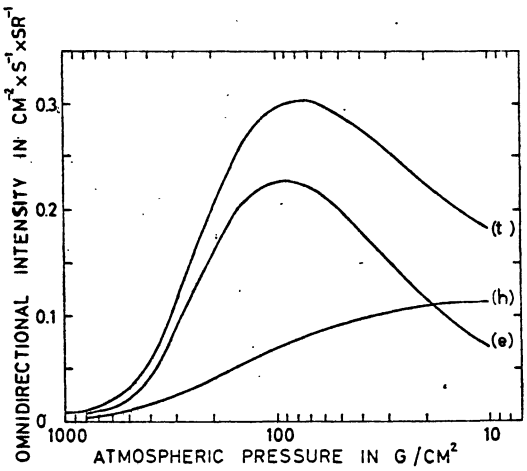

Figure 3. Electron intensity in the atmosphere (e), total charged particle flux (t), hard component (h), (Brini et al. 1967).

flight than on Verma's. However, a comparison of Figures 1 and 2 with Figure 3 indicates the opposite. Either the electrons are very anisotropic or there is an error in normalization in one or the other of the measurements.

Multiplication of Verma's intensities by a factor of $\alpha \simeq .4$ bring the two measurements into close agreement. Recently, Israel (1969) has published evidence that Verma's results do indeed need correction by about this amount. Letting $\alpha = .4$, we shall modify equations (8a-d) to obtain a better estimate of the omindirectional electron flux over each hemisphere. The expressions will now read:

$$i_{down}(p) = 5.6 \times 10^{-3}\ cm^{-2}\ sec^{-1}\ sr^{-1} \quad (0<p<10mb) \qquad (11a)$$

$$i_{down}(p) = 2.4 \times 10^{-3}\ p^{.83}\ cm^{-2} sec^{-1}\ sr^{-1} \quad (0<p<100\ mb) \qquad (11b)$$

$$i_{up}(p) = 2.8 \times 10^{-3}\ e^{.01p}\ cm^{-2} sec^{-1}\ sr^{-1} \quad (0<p<80mb) \qquad (11c)$$

$$i_{up}(p) = 2.8 \times 10^{-3}\ e^{.80}\ cm^{-2}\ sec^{-1}\ sr^{-1} \quad (80<p<120\ mb) \qquad (11d)$$

In order to gain a better approximation to the electron flux, one must wait for a resolution of the conflicting claims and more detailed measurements of the variation of the electron intensity and energy spectrum with depth and zenith angle. In the absence of such data, we shall take the gamma ray production in each hemisphere to be isotropic to first approximation. We shall later make a correction for the enrichment of the

downward electron intensity near 90^{o} zenith angle). In any case, the intensity and energy spectrum of the computed atmospheric gamma ray background is far more sensitive to changes in the electron intensity and energy spectrum than to the form of the electron angular distribution. The normalization (equation 11a-d) and energy spectrum (10a-d) which we have postulated from a consideration of several experiments will be supported in a later chapter by an independent check a comparison of our computed atmospheric background with observations made by Peterson and Schwartz (Figure 16).

3b The Radiated Gamma Ray Spectrum

From the assumed electron spectrum one can obtain the radiated gamma ray spectrum. If we take the electron flux to be isotropic over each hemisphere and the bremstrahlung to be forward, the rate of production of gamma rays in a small volume element of atmosphere with cross sectional area ΔA and thickness Δp, into a small energy interval ΔE_{γ}, and into a small element of solid angle $\Delta\Omega$ is given by

$$dn_{\gamma}(E_{\gamma},p) = \int j_{e}(E_{e},p)\,\Phi(E_{e},E_{\gamma})dE_{e}\,\Delta E_{\gamma}\Delta p\Delta A\Delta\Omega \qquad (12)$$

where $j_{e}(E_{e},p)$ is the upward (or downward) differential electron flux at depth p, as determined by equations (8a,b), (11a,b), (10a-d); $\Phi(E_{e},E_{\gamma})$ is the differential cross-section for the production of a gamma ray of energy E_{γ} from an electron of energy E_{e} in cm^{2}/gram of air.

Since the postulated electron energy dependence does not vary with altitude, neither will that of the bremstrahlung production. I.e., the pressure dependence in the right hand side of (12) can be factored out. The cross-sections $\Phi(E_e,E_\gamma)$ were calculated by Bethe and Heitler (1934). If E_0 is the total energy of the incident electron and E_γ is the radiated photon's energy, the scattered electron energy will be $E = E_0 - E_\gamma$. Now let us define

$$v = E/E_0,$$

$$\gamma = \frac{100mc^2E}{E_0EZ^{1/3}}$$

$$k = \frac{4Z(Z+1)}{137}\left(\frac{e^2}{mc^2}\right)^2$$

For air, $\gamma \simeq 26.4E/E_0E$ and $k \simeq 1.4 \times 10^{-25}$ cm^2; then we have

$$\Phi(E_0,E_\gamma)dE_\gamma = k\, dE_\gamma/E_\gamma \left[(1+v^2-2v/3)\log(2E_0E/E_\gamma mc^2) - \tfrac{1}{2} - c(\gamma)\right] \quad \gamma>2 \tag{13a}$$

where $c(\gamma)$, as calculated by Bethe and Heitler, decreases monotonically from .21 at $\gamma = 2.0$; it is usually neglected for $\gamma > 15$. For small γ,

$$\Phi(E_0,E_\gamma)dE_\gamma = k\frac{dE_\gamma}{E_\gamma}\left\{(1+v^2)\left[\frac{\Phi_1(\gamma)}{4} - 1/3\ \log Z\right] - 2/3v\left[\frac{\Phi_2(\gamma)}{4} - 1/3\ \log Z\right]\right\} \quad \gamma<2 \tag{13b}$$

which reduces to

$$\Phi(E_0,E_\gamma)dE_\gamma = k\frac{dE_\gamma}{E_\gamma}\left[(1+v^2-2v/3)\log 183Z^{-1/3} + v/9\right] \tag{13c}$$

for $\gamma \simeq 0$. $\phi_1(\gamma)$, $\phi_2(\gamma)$ are correction terms calculated by Bethe and Heitler: both lie between 16 and 21 for all values of γ. These bremstrahlung cross-sections of electrons off the field of the nucleus (we have included the atomic electrons by a simple redefinition of k: the substitution of a factor (Z + 1) for Z) were derived under the assumption that $E_0 >> mc^2$.

At the energies below about E_0 = 3 Mev, one would expect that that assumption would begin breaking down. The bremstrahlung from electrons in the 1 Mev to 3 Mev range constitute a small but significant fraction of the low energy gamma rays. Although no analytic expressions for the cross-section in this region exist, we can estimate this contribution by the extrapolation of equations (13). If we include the lower energy electrons in this way, we find that the production of bremstrahlung photons of energy 300 kev increases by 20%. The contribution at higher photon energies is correspondingly less and is zero, of course, for E_γ greather than 3 Mev. Because the correct extrapolation is expected to have the rough logarithmic energy dependence of (13a), it is estimated that the extrapolation of equations (13) to $E_0 \simeq 1$ Mev will introduce no errors greater than 10% in the calculated bremstrahlung production spectrum (See, e.g., the discussion in Evans,1955). Because of the energy degradation of the gamma rays by Compton scattering in the atmosphere, the error in the predicted flux

at balloon altitude will be only about half as great.

The shape of the bremstrahlung production spectrum, as calculated from (10), (12) and (13), for upward moving bremstrahlung is shown in Figure 4. The shape of the downward spectrum is nearly the same. The normalization is fixed by the same equations along with (8a,b) and (11). The rate of photon production in the energy region $.3 < E_\gamma < 100$ Mev in a column of atmosphere 1 cm^2 in area is

$$I_{up} = 7.3\ \gamma\text{-rays/cm}^2\ \text{sec} \qquad 0 < p < 120\ \text{mb} \tag{14a}$$

$$I_{down} = 6.7\ \gamma\text{-rays/cm}^2\ \text{sec} \qquad 0 < p < 100\ \text{mb} \tag{14b}$$

3c. The Bremstrahlung Flux at Balloon Altitude

In the preceding section, a simplified model of the bremstrahlung source function was developed. It is now possible to simulate the production of photons weighted by this source function, trace their paths according to the Monte Carlo program ATMSCAT of Part A, and thereby obtain the low energy gamma ray flux due to bremstrahlung at 3.5 mb.

For the case of upward moving electrons, each photon was chosen randomly, but weighted according to; the energy distribution of Figure 4, the depth distribution of (11c,d), an isotropic angular distribution over the upper hemisphere. The photons generated in this way were followed by ATMSCAT. The analogous procedure was employed for downward moving electrons.

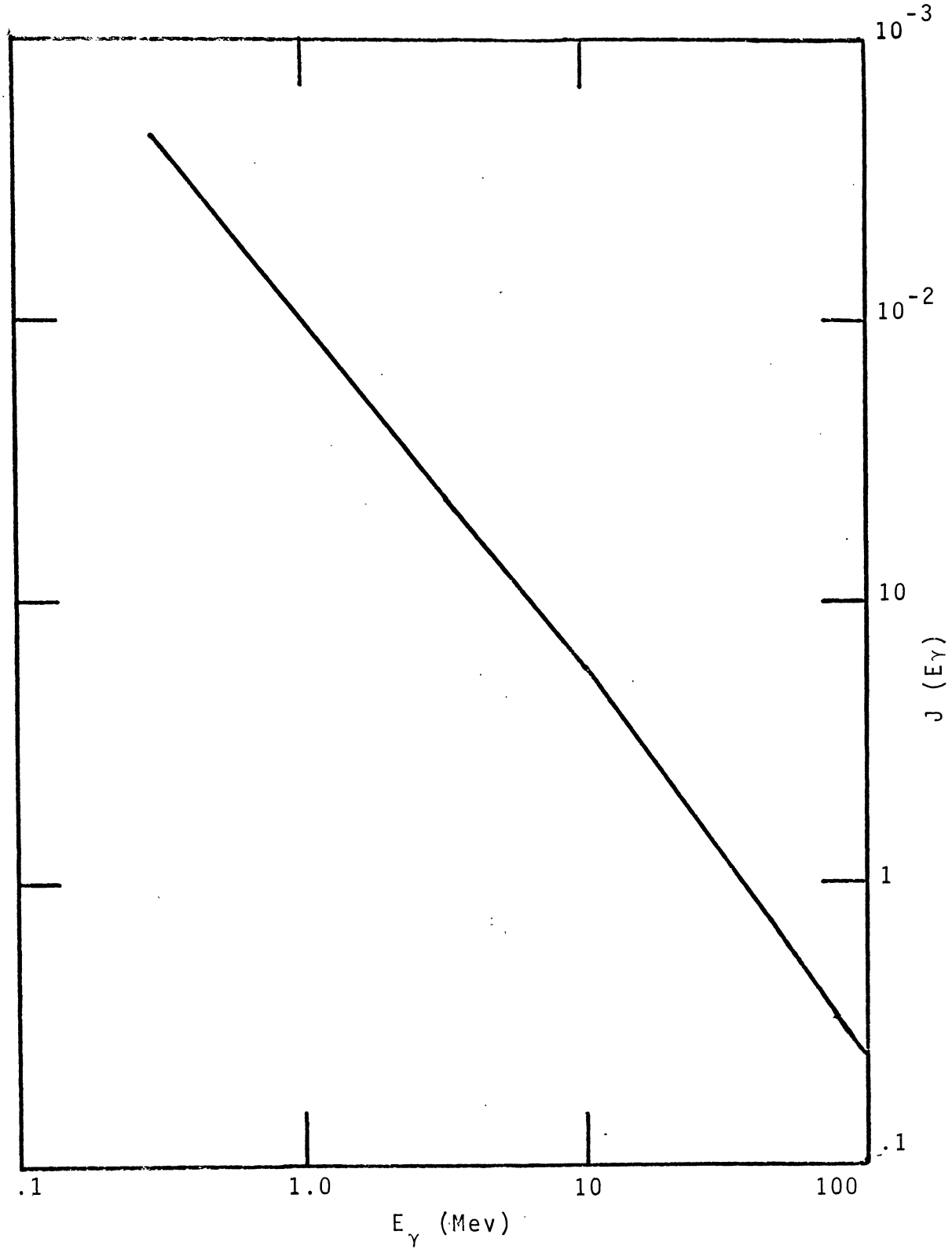

Figure 4. Production spectrum of upward bremstrahlung. Differential energy intensity (arbitrary units) vs. gamma ray energy.

If an "event" is defined by a simulated gamma ray crossing 3.5 mb with energy between 300 kev and 10 Mev (at the time of crossing), then over 30,000 events were obtained for upward and downward moving electrons, respectively. The events were stored in 100 kev x 15^{o} energy-angle bins.

Let b_i (E) be the number of events contained in the i^{th} angular bin and in some fixed energy interval Δ E, which may contain more than one 100 kev energy bin. Let N be the total number of gamma rays simulated, $\Delta\Omega_i$ be the solid angle subtended by the i^{th} bin, with α_{i1} and α_{i2} the respective lower and upper bounds to the zenith angle for that bin. Then with the overall normalization I_o fixed by (14a, b), we can write

$$dI_\gamma/d\Omega_i \simeq I_o \frac{b_i\ (\Delta E)}{N}\left[\int_{\alpha_{i1}}^{\alpha_{i2}} d\Omega_i \cos\alpha\right]^{-1} (cm^{-2}s^{-1}sr^{-1}) \qquad (15)$$

where $d\Omega_i$ is an infinitessimal element of solid angle contained in the finite sized bin $\Delta\Omega_i$, the cos α factor in the integral is necessary to adjust for the orientation of the flat surface at 3.5 mb with respect to the incident photon direction.

The denominator of (15) is easily found to be

$$\int_{\Delta\Omega_i} d\Omega_i \cos\alpha = 2\pi\left|\frac{\sin^2\alpha_{i1} - \sin^2\alpha_{i2}}{2}\right| \qquad (16)$$

Letting Δ E range over the entire .3 Mev to 10 Mev band, the angular distribution of low energy gamma rays of bremstrahlung origin can be obtained from (15) and (16). The calculated fluxes are displayed in Figure 5.

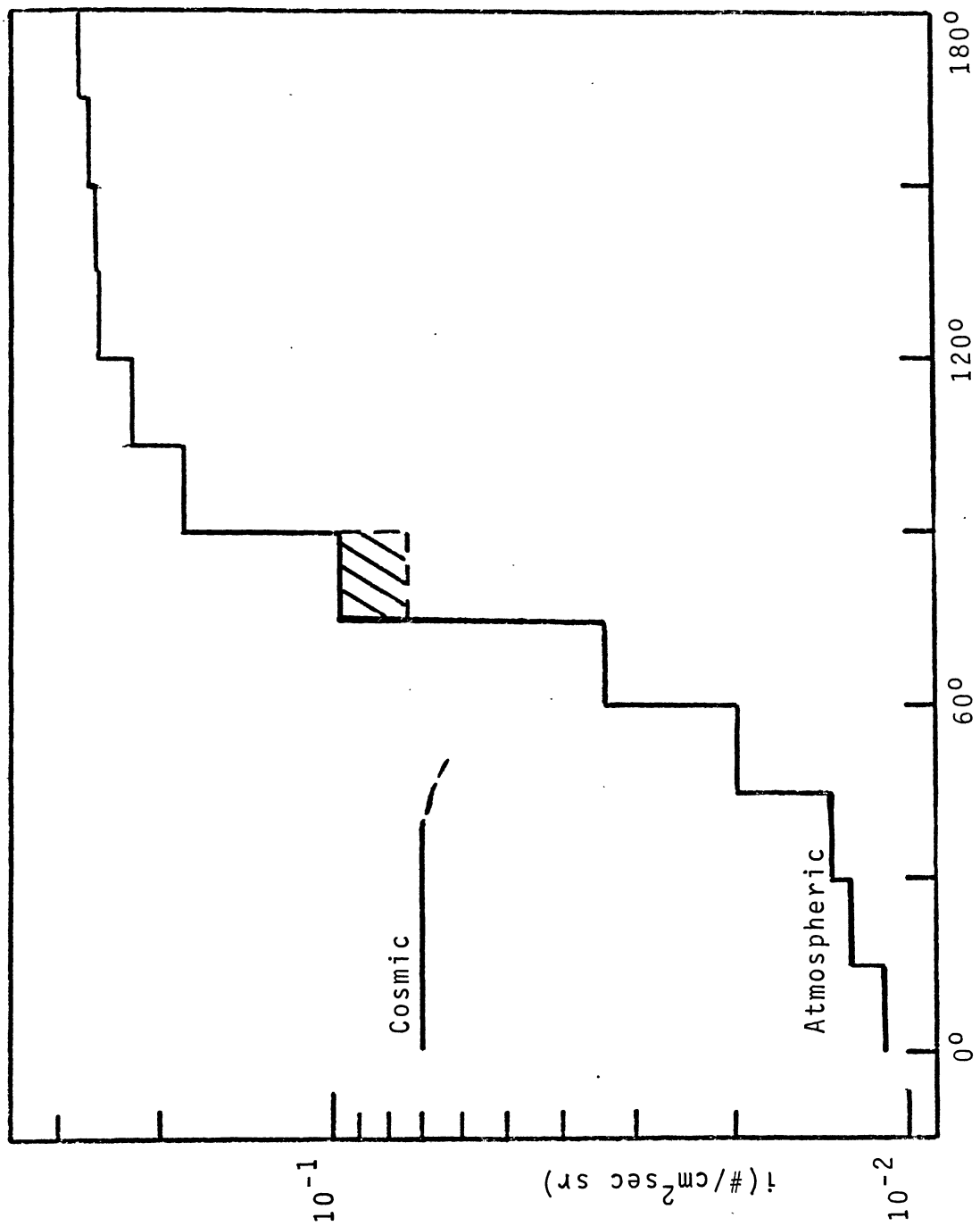

Fig. 5. Intensity of atmospheric bremstrahlung vs. zenith angle.

The overall features of the Figure 5 can be qualitatively understood by noting that in the approximation of no deflection by scattering, the photon intensity in a particular direction is roughly proportional to the product of electron intensity (in that direction) times the amount of atmosphere, integrated out to some average critical absorption length. Because the upward electron intensity increases with depth, there is a slight peaking towards the vertical in the calculated upward gamma ray flux: the average upward electron directional flux over an interaction length is maximum at the vertical. If the electron upward flux is itself peaked towards the vertical, the peaking in the upward bremstrahlung would be enhanced.

Even if the downward moving electrons were completely isotropic over the hemisphere, the downward photon flux near the top of the atmosphere would still be skewed towards 90^{o}. This is the standard "sec θ effect", following from the augmented path length that electrons at large angles have in which to radiate. However, the electrons themselves may be anisotropic. If one assumes that the downward electron flux satisfies

$$j\ (p,\alpha) = j\ (p/\cos\alpha, 0)$$

near the top of the atmosphere, then the depth dependence for the vertical flux, as indicated by Figure 2, can be used to arrive at the angular distribution of electrons.

Above 3.5 mb altitude, the electron distribution will be rather flat between 0^o and 75^o, but will increase considerably between 75^o and 90^o. This adds an extra contribution to the gamma ray flux near 90^o - the size of the correction is indicated by the shaded area in Figure 5. The illustrated shading is an average over the solid angle bin. The correction necessary in any small solid angle bite $d(\cos\alpha)$ is roughly proportional to the excess electron flux in that infinitessimal interval integrated over one gamma ray absorption length, which we take to be $\lambda_\gamma \simeq 20 g/cm^2$, from 3.5 mb towards the top of the atmosphere in the direction. From this we find that the maximum correction is required at $\alpha \simeq 89^o$, corresponding to a path-length of $\sim 150 g/cm^2$ from the top of the atmosphere to the detector - the correction there is about six times the average (in the bin). At larger angles still, there is a cut-off in electron intensity and a resulting decrease in computed photon flux.

The omnidirectional intensity over a hemisphere is obtained from (15) by

$$I_\gamma = \sum_i \frac{dI_\gamma}{d\Omega_i} \Delta\Omega_i \qquad (17)$$

where the summation is over each of the six bins in the hemisphere. Noting that,

$$\Delta\Omega_i = 2\pi\left|\cos\alpha_{i1} - \cos\alpha_{i2}\right| \tag{18}$$

and then combining equations (15) - (18)

$$I_\gamma = \frac{2I_0}{N} \sum_i \frac{b_i(\Delta E)}{\left|\cos\alpha_{i1} + \cos\alpha_{i2}\right|} \text{ cm}^{-2} \text{ sec}^{-1} \tag{19}$$

Intensity versus energy curves are plotted in Figure 6 for upward and downward moving photons. It should be noted that, because of deflection through Compton scattering, the upward (downward) bremstrahlung flux is not entirely due to upward (downward) moving electrons. The error bars in Figure 6 correspond to one standard deviation resulting from statistical fluctuations in the $b_i(\Delta E)$.

4. Positron Annihilation

Because about 85% of all atmospheric positrons annihilate from rest (Lowder 1969), the source function for annihilation radiation is approximately a delta-function of energy and isotropic over 4π steradians:

$$S(E, \Omega, p) = \frac{s(p)}{4\pi} \delta(E - .511 \text{ Mev}) \tag{20}$$

where s(p) is a function of depth only. Rocchia (1966) has investigated the depth dependence of s(p) and found it to vary as

$$s(p) \sim e^{-p/170} - .75e^{-p/75} \tag{21}$$

with p expressed in mb. Since we are interested in the flux at 3.5 g/cm^2 residual pressure and the interaction length for

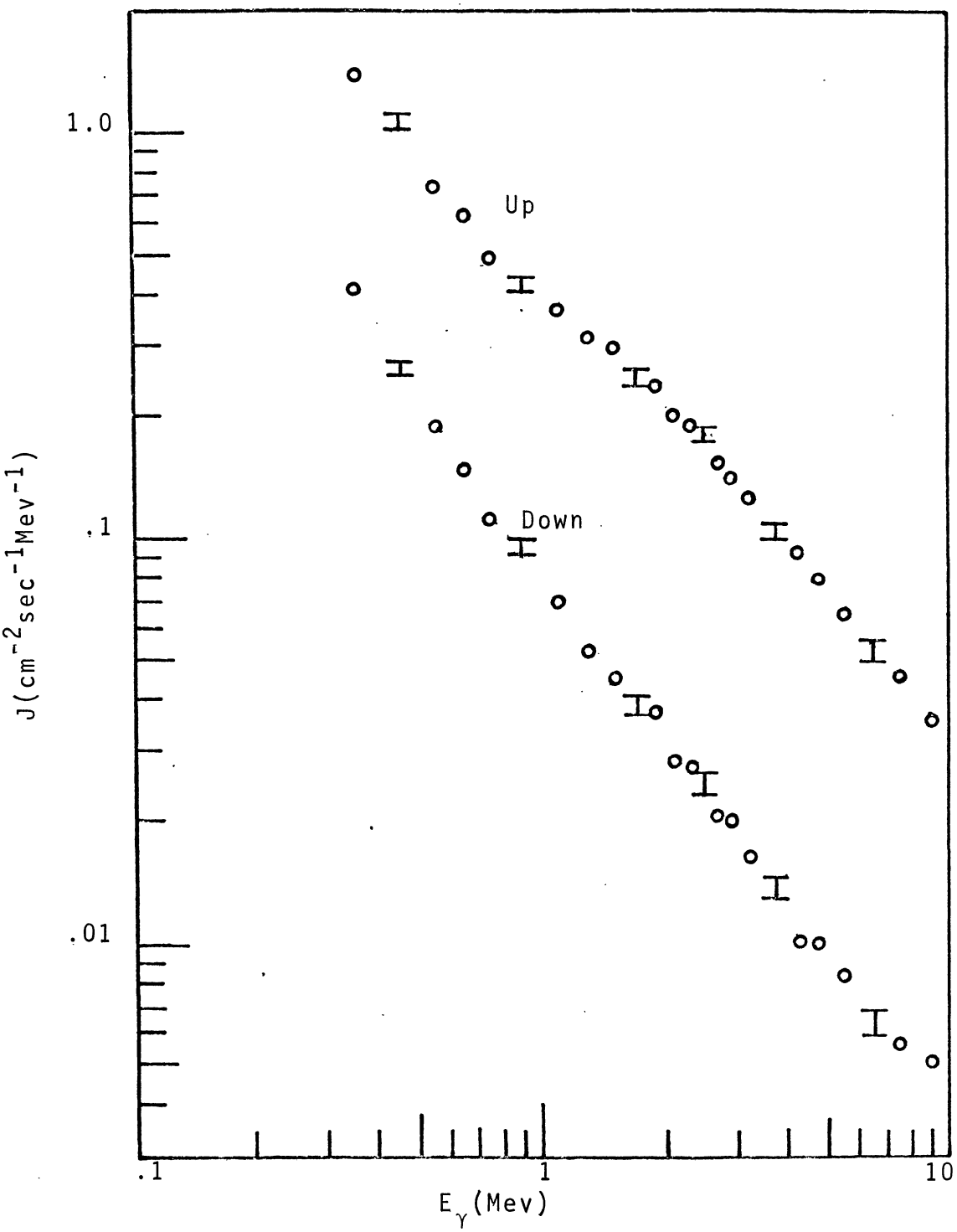

Figure 6. Bremstrahlung intensity at 3.5 mb.

a .511 Mev photon is only about 11.5 g/cm^2, the source function is nearly constant over the altitude range of interest. This, along with the isotropy of production, implies that the upward flux of .511 Mev photons near the top of the atmosphere is very nearly isotropic.

Employing the source function of (20) and (21) in the Monte Carlo program and normalizing the results to the measured annihilation line strength at balloon altitude (Chupp,etal. 1969):

$$I_\gamma(.511 \text{ Mev}) \simeq .2 \text{ cm}^{-2} \text{ sec}^{-1}, \tag{22}$$

we are able to estimate the up-down asymmetry:

$$I_{\gamma up}(.511 \text{ Mev}) \simeq .14 \text{ cm}^{-2} \text{ sec}^{-1} \tag{23a}$$

$$I_{\gamma down}(.511 \text{ Mev}) \simeq .06 \text{ cm}^{-2} \text{ sec}^{-1} \tag{23b}$$

and the contribution of scattered annihilation radiation to the continuum flux at 3.5 mb (Figure 7). A comparison of Figure 7 with Figure 6 indicates that this radiation constitutes a significant part of the background intensity below .5 Mev.

5. Nuclear De-excitation

The dominant set of reactions for producing nuclear line radiation in the atmosphere is fast neutron ($E_n \gtrsim 1$ Mev) inelastic scattering:

$$n + N^{14} \longrightarrow N^{14} + n + \gamma \tag{24a}$$

$$n + O^{16} \longrightarrow O^{16} + n + \gamma \tag{24b}$$

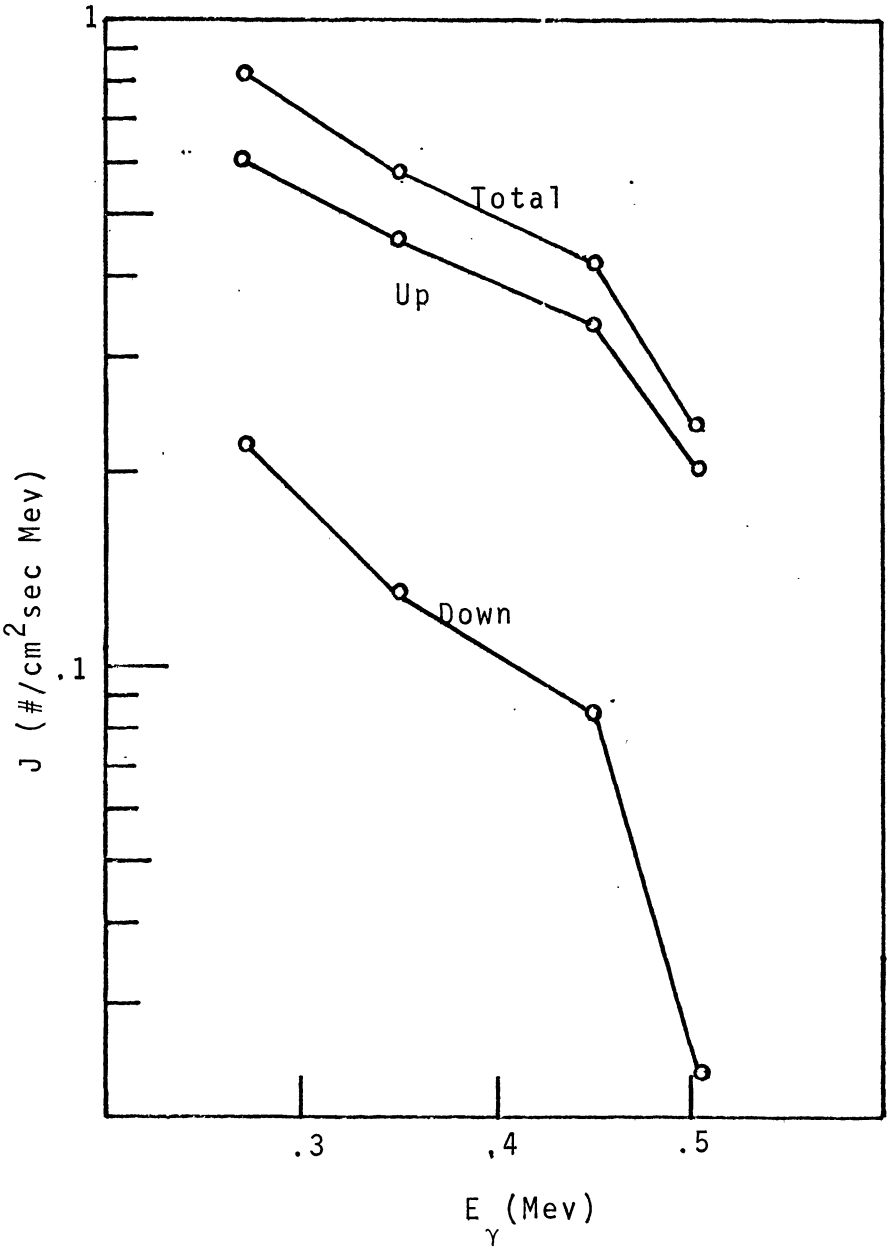

Figure 7. Scattered Annihilation Radiation at 3,5 mb.

The incident neutron interacts with an air nucleus, a neutron (above $E_n \sim 10$ Mev, there may be two or more neutrons) reemerges, leaving the target nucleus in an excited state. One or more photons are then emitted as the nucleus returns to the ground state. For a general discussion of these processes, see (Guernsey and Lind 1961).

No detailed measurements of the angular distribution of gamma rays with respect to the incident neutron direction are in existence for either Nitrogen or Oxygen targets. However, if the interference between states during scattering is small, a simple quantum mechanical argument shows that the differential cross-section is symmetric about 90^o. For light nuclei the levels are widely spaced and the assumption quoted above should be good. From this symmetry and the overall diffuseness of neutrons in the atmosphere, it is reasonable to take the gamma ray source function for nuclear de-excitation to be isotropic. If the energy dependence of the neutron flux is taken to be constant over the altitude range of interest, one can write the source function as a summation over the possible lines

$$S(E,\Omega,p) = \frac{s(p)}{4\pi} \sum_j \delta(E-Ej)\ a_j \qquad (25)$$

in analogy with equation (20).

At depth p^* the intensity of the j^{th} line is given by

$$I_\gamma(E_j) = \frac{\alpha}{2}\int dp \int_0^1 \frac{d\mu}{\mu} e^{-|p-p^*|\sigma_\gamma(E_j)/\mu} \int dE_n J_n(E_n,p)\sigma_n(E_n,E_j) \qquad (26)$$

with

α = the mole fraction of the target nucleus, .78 for N^{14}, .21 for O^{16}.

$\sigma_\gamma(E_j)$ = the total cross-section (in cm^2/gram) for a photon of energy E_j in air.

$J_n(E_n,p)$ = the differential neutron energy flux as a function of energy and depth.

$\sigma_n(E_n,E_j)$ = the cross-section (in cm^2/gram) for a neutron of energy E_n to inelastically scatter in a medium of pure target atoms with the production of a photon of energy E_j.

The neutron flux in the energy range (1 Mev$<E_n<$14 Mev) was investigated by Haymes (1964). At $\lambda = 41.5^o$, it was found to vary as

$$J_n \sim f(p)\, E_n^{-1.3} \quad cm^{-2}\, sec^{-1}\, Mev^{-1}$$

where f(p) is a function of altitude only. The normalization of the neutron flux as a function of depth can be estimated from the measurements of Haymes (Figure 8). The primary difficulty in evaluating the integral expression (26) is the scarcity of information on neutron inelastic cross-sections.

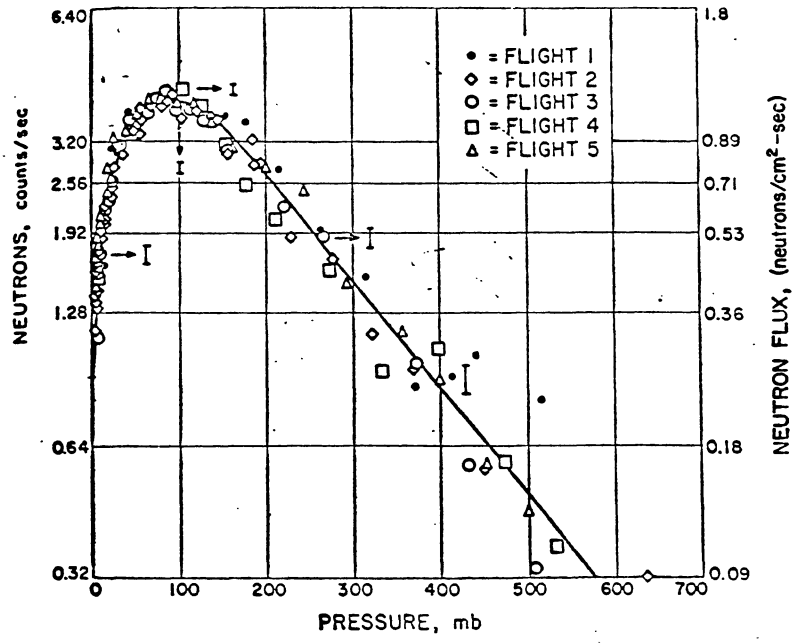

Figure 8. Neutron Flux vs. Altitude (Haymes 1967).

From the limited data on inelastic scattering of neutrons, it appears that the 6.13 Mev O^{16} line should stand out the strongest. Fortunately, the data for this process is less sparse than for most of the nitrogen and oxygen lines. The measurements are summarized in Figure 9. There is a gap in the peak region about 12 Mev. By a subtraction of competing inelastic processes from the total inelastic cross-section in this energy region (Hughes and Schwartz 1964), we estimate the cross section for production of the 6.13 Mev line to be 375±100 mbarns at E_n = 12 Mev.

A numerical integration of the expression (26) yields the intensity of the 6.13 Mev line at p^* = 3.5 mb:

$$I(6.13 \text{ Mev}) \simeq 6.4 \times 10^{-3}/\text{cm}^2 \text{ sec} \qquad (27a)$$

From measurements of Hall and Bonner (1959) of the inelastic scattering of neutrons in nitrogen below 8.2 Mev, lower limits can be placed on the strengths of other lines. At 3.5 mb pressure the largest of these lower limits is

$$I(2.3 \text{ Mev}) \gtrsim 2.2 \times 10^{-3}/\text{cm}^2 \text{ sec} \qquad (27b)$$

Although, as discussed later, these and other lines may be detectable, they make up at most a few percent of the total gamma ray intensity at balloon altitude. From Monte Carlo simulations, it can be asserted that this remains true with the inclusion of Compton degraded de-excitation photons.

Gamma rays can also be generated in slow neutron capture reactions in the atmosphere, specifically $N^{14}(n,\gamma)N^{15}$.

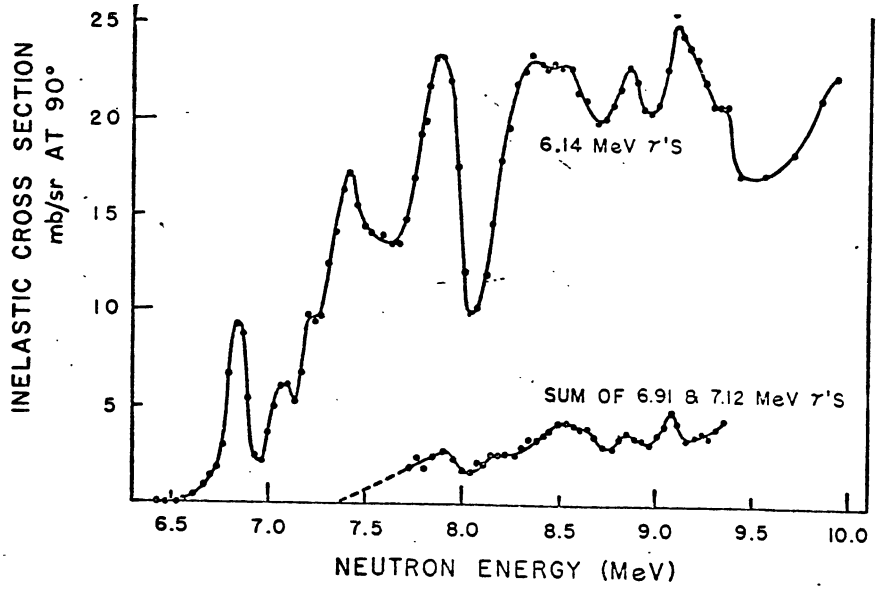

(Hall and Bonner 1959).

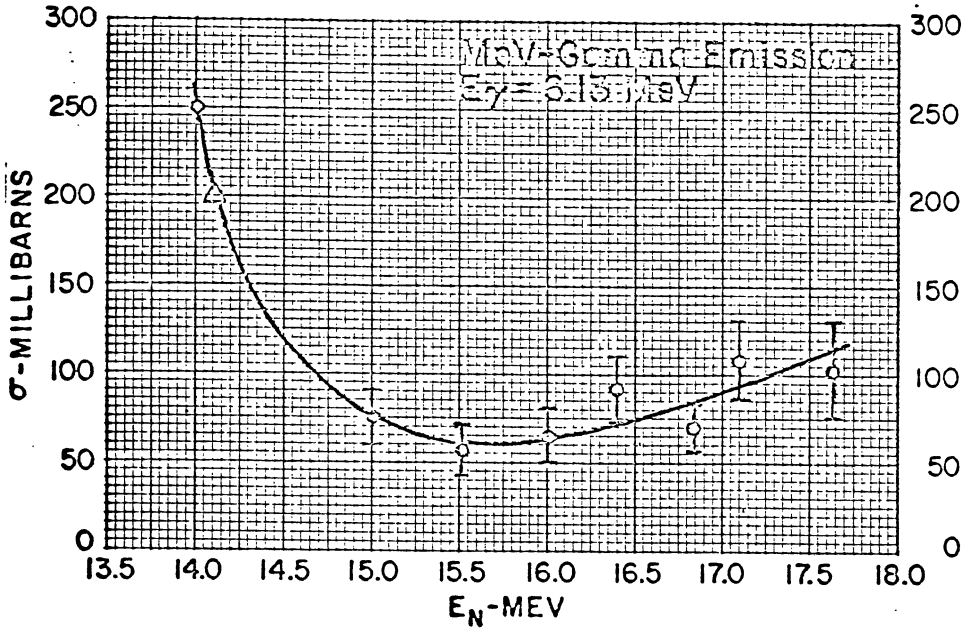

(Hughes and Schwartz 1964).

Figure 9. Neutron Inelastic Scattering in O^{16}.

Vette (1962) has shown this source to be very weak. The dominant capture reaction, $N^{14}(n,p)C^{14}$ is about 20 times more probable (Hughes and Schwartz 1958). Since the total neutron absorption rate in a column of atmosphere is approximately $3.5/cm^2$ sec (Kouts and Yuan 1952), and since the photon multiplicity is about two for light elements (Muehlhause 1950), the gamma ray production rate is of the order of $.35/cm^2$ sec in the column. If the slow neutrons are assumed to be distributed uniformly per gram of atmosphere, then since the interaction length of a photon is less than 40 g/cm^2, the flux of gamma ray lines at the top of the atmosphere due to the capture of slow neutrons is

$$I_\gamma \lesssim \tfrac{1}{2}(.35)(40/1000) \tilde{=} 7 \times 10^{-3}/cm^2 \text{ sec} \qquad (28)$$

The radiation is distributed among a multitude of different lines so that the intensity of any one line is miniscule. Monte Carlo simulations indicate that the intensity will no more than double if Compton degraded photons are included. From (28) and Figure 6, it can be concluded that capture reactions account for less than1% of the gamma ray flux at balloon altitude.

6. Gamma Rays from π^o -Decay

Mesons are copiously produced in cosmic ray collisions with atmospheric nuclei. Gamma rays are then created through the decay channel:

$$\pi^o \longrightarrow 2\gamma$$

where each photon has 70 Mev of energy in the rest frame of the pion. Since the pions are often highly relativistic, it is quite possible to have gamma rays with energies below 10 Mev being created in this way. Stecker (1967) has pointed out that, if plotted versus log E_γ, the differential energy spectrum of the decay photons is symmetric about log $(\frac{1}{2}m_\pi c^2)$. Furthermore, higher energy photons can be degraded by scattering to less than 10 Mev.

A calculation of cosmic ray production of π^0's at 4.5 GV cut off has been carried out by Perola and Scarsi(1966). They were able to obtain an estimate of the spectrum of pions generated by the incident cosmic ray flux passing through one gram of air.

From this pion spectrum, one can construct a gamma ray source function. The incident flux of cosmic rays is taken to be isotropic downwards, and following Perola and Scarsi, the absorption length of these particles to be 95 g/cm^2. If some assumption is then made for the angular distribution of pion production with respect to the incident direction, one has a source function for pions.

Pions are then chosen by Monte Carlo according to the weight of the source function. Each pion is allowed to decay isotropically in its rest frame into two 70 Mev photons. The gamma rays are mapped via the Lorentz transformations back to the lab system where they can be followed by ATMSCAT and

the flux at balloon altitude determined.

The procedure outlined above was followed with two different models of pion production:

(a) The pions are produced collinear with the incident particle.

(b) The pions are produced isotropically.

In neither case is the computed low energy gamma ray flux at balloon altitude appreciable compared with the bremstrahlung. The flux of π^0-decay gamma rays between 7 and 10 Mev is calculated to be less than 1% that due to bremstrahlung; at lower energy, of course, the ratio becomes rapidly smaller.

The π^0-production was not followed beyond the first strong interaction. The charged pions coming off from these collisions in the upper atmosphere decay before encountering nuclei:

$\lambda_{decay} < 10^{-3} \lambda_{nuclear}$ $(E_\pi \lesssim 1.5$ Bev$)$

at 40 kilometers.

On the average, over half the incident particle's energy goes into pion production for incident energy below 100 Bev. (Sandstrom 1965, Hayakawa 1969). The degraded nucleons are considerably less efficient in producing low energy gamma rays than the primary particles. The multiplicity of pion production is lower, and more significantly, the pions arising from secondary collisions are typically of lower energy; it is only the pions above about 1 Bev that can

have a low energy gamma ray as a decay product. Moreover, secondary collisions will typically occur at greater depths than primary interactions, with the resultant gamma rays more likely to be absorbed before traversing a flat surface at 3.5 g/cm^2. We conclude that the contribution to the low energy gamma ray flux at balloon altitude from secondary strong interactions will also be less than 1%.

It is of interest to extend the results of this section and Part 3 to higher energies. In Figure 10, the contributions of bremstrahlung and π^o-decay to the gamma ray intensity at 3.5 g/cm^2 is plotted versus energy. From the discussion above, it is clear that the π^o-decay curve must be viewed with caution as the energy is increased toward $E_\gamma \tilde{} 70$ Mev.

7. Total Atmospheric Background

The computed total flux of atmospherically produced low energy gamma rays at 3.5 g/cm^2 residual pressure is shown in Figure 11. Estimates of the respective contributions of the various process are summarized in Table 3 which follows.

Table 3

.3-10 Mev Photon Flux at 3.5 mb

Process	(#/cm^2sec)	Fraction of Total
Bremstrahlung	1.7	84%
.511 Mev Line	.20	10%
Scattered .511 Mev	.10	5%
Nuclear De-excitation	>.01, <.05	>5% <3%

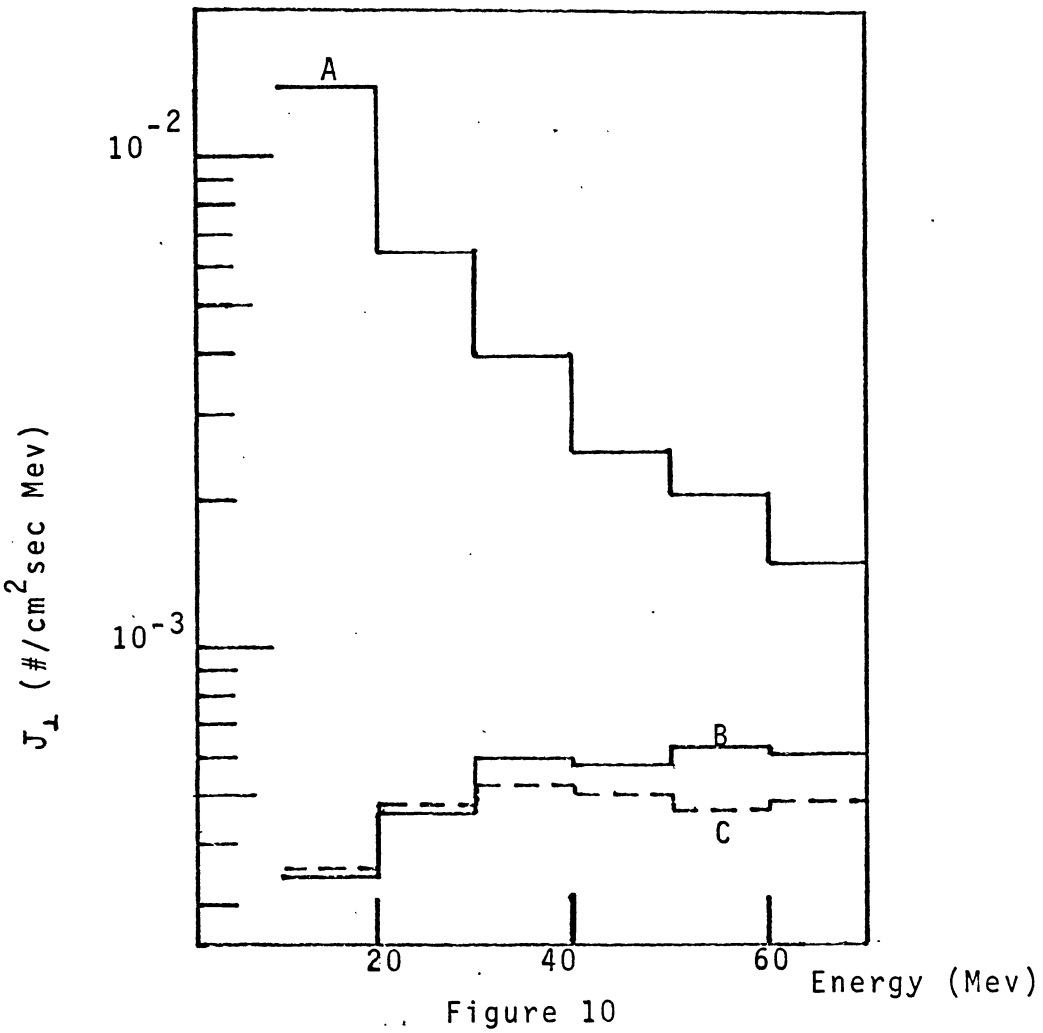

Figure 10

Medium Energy Gamma Rays
Through a Flat Area at 3.5 Mb

A Bremstrahlung

B π^o (Isotropically Produced) Decay

C π^o (Forward Produced) Decay

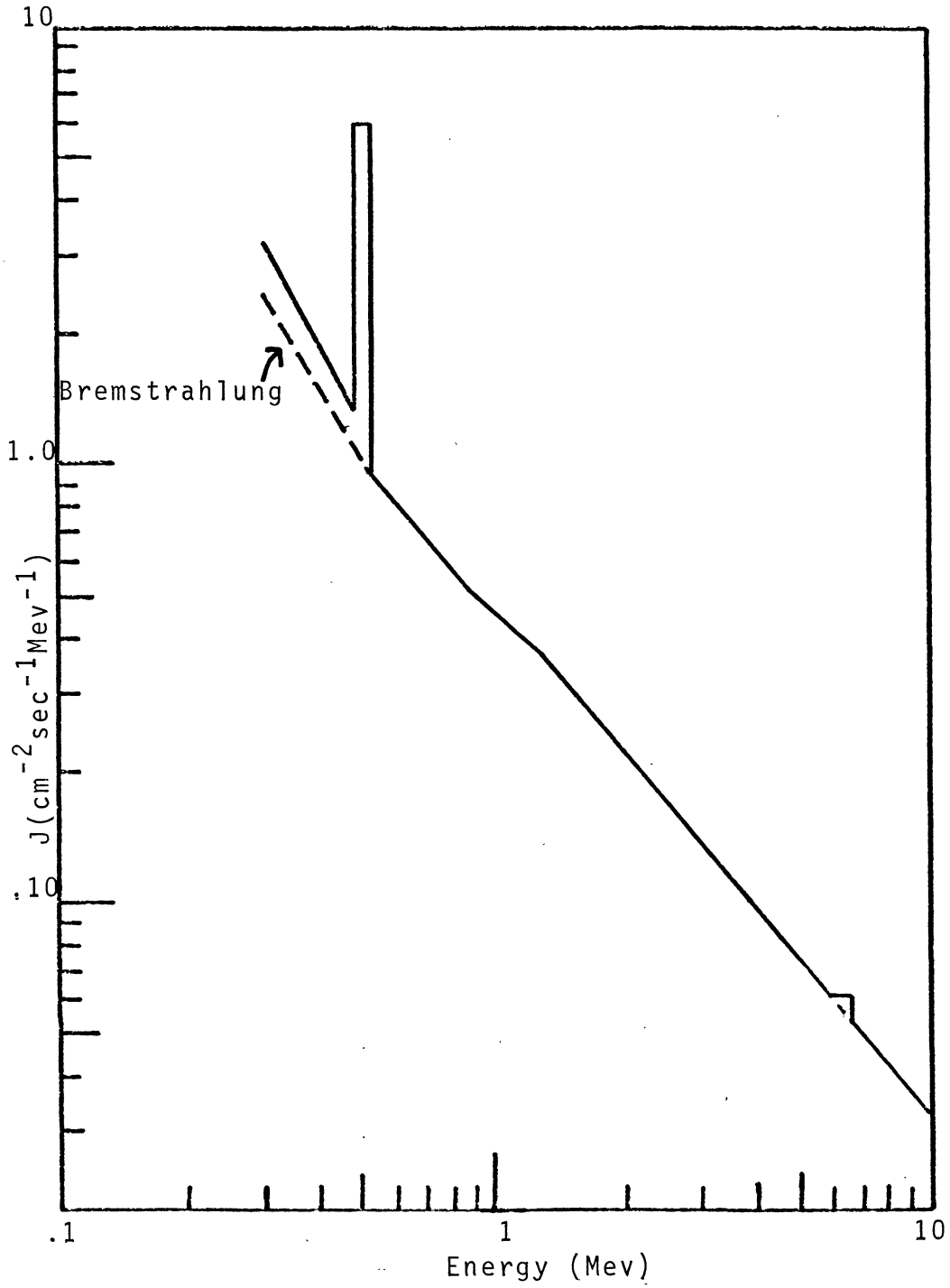

Figure 11. Total Atmospheric Low Energy Photons at 3.5 mb.

CHAPTER III

A LOW ENERGY GAMMA RAY INSTRUMENT

Under development here, in the Gamma Ray Laboratory at S.A.O., is an instrument to be used in the investigation of low energy gamma rays from space. The heart of the detector is a cylindrical 3" diameter x 3" thick NaI(TI) crystal coupled to a ten stage R.C.A. photomultiplier. The crystal was manufactured and packaged by Harshaw Chemical Co. The phototube output is amplified and then fed into a 1024 channel analogue to digital converter purchased from Nuclear Data,Inc. The energy resolution of the system is 7.5% at .66 Mev.

Pulses resulting from charged particles passing through the crystal are rejected by anti-coincidence with the output of another phototube, which is optically coupled to a thin plastic scintillation shield completely surrounding the No. I detector and its tube. The background is kept to a minimum by having the electronics and power source encased in a separate gondola, well away from the detector.

A gamma ray event is classified in the ADC according to pulse-height with the result being stored as a binary integer in a sequence of flip-flops. The bits are sampled by a parallel to serial converter and telemetered to ground via pulse-code modulation. At the receiving station, the pulse-height bits are stored on magnetic tape, along with the time in

milliseconds, for future analysis.

The purposes of preliminary flights are:

(a) To compare the atmospheric gamma ray background at Hyderabad, India, 16.9 GV vertical cut-off rigidity, with the background at 4-5 GV cut-off.

(b) To search for gamma rays from a solar flare, and if successful, to make a detailed time profile comparison of the gamma ray spectrum with other flare parameters.

(c) To look for periodic gamma ray bursts from pulsars.

There have been three attempts to date at balloon launchings with this instrument aboard. First, at Hyderabad in March 1969, there was an initiation command error and the payload separated from the balloon at launch. Second, at Holloman A.F.B., New Mexico in October 1969, a pressure leak developed, and during ascent break-down in the tube base ensued with a resulting severe loss in gain. Finally, again at Hyderabad, March 1970, the transmitting antenna was broken off in launching and the data was lost

In order to properly interpret future observations made with this instrument, it is necessary to examine in some detail, the response of cylindrical NaI detectors to gamma ray fluxes.

Moreover, such an analysis will allow a comparison of the calculations of Chapter II with experimental results that have been obtained.

CHAPTER IV

DETECTOR RESPONSE

A. Processes in the Crystal

After entering the crystal detector volume, a gamma ray can:

1. Compton scatter
2. Pair produce
3. Undergo photo-electric absorption
4. Pass through unaltered

If it scatters, the secondary photon can do any of the above things, etc.; the recoil electron is slowed by ionization losses, but may radiate before stopping, thereby compounding the problem. Similar remarks are applicable to pair production and photo-electric absorption. Also, in the case of pair production, the positron will usually annihilate from rest in the crystal with the creation of two .511 Mev photons.

The light output from the crystal for a single event is approximately proportional to the energy deposited by electron ionization in the detector. However, as outlined above, some of the gamma ray energy may escape the detector volume. Furthermore, the recorded pulse-height is not strictly proportional to the energy losses in the crystal. There are small non-linearities in light output and the usual flucuations in

the number of electrons being emitted from the photocathode. The statistics are Poisson in nature, with the resolution of the system being nearly proportional to the square root of the energy loss. Improvement in energy definition can be obtained by better light collection and higher photocathode efficiency.

The pulse height distributions resulting from several equal intensity monoenergetic gamma ray sources are displayed in Figure 12. Typically, there is a nearly Gaussian peak corresponding to events where the entire energy of the incident photon E_γ is absorbed and a continuum of pulse-heights up to a fairly sharp cut-off corresponding to maximum energy transfer to a recoil electron in single scattering. This cut-off is termed the Compton edge and falls at:

$$E_c = E_\gamma - \frac{E_\gamma}{1 + 2E_\gamma/mc^2} \qquad (1)$$

where m is the mass of the electron. If the quantum energy is above $2\ mc^2$, there are bumps corresponding to annihilation radiation escape at

$$E_1 = E_\gamma - mc^2 \qquad (2a)$$

and

$$E_2 = E_\gamma - 2mc^2 \qquad (2b)$$

There are other features resulting from interaction with the surrounding material. In particular, at .511 Mev and near the "back-scattered peak" at

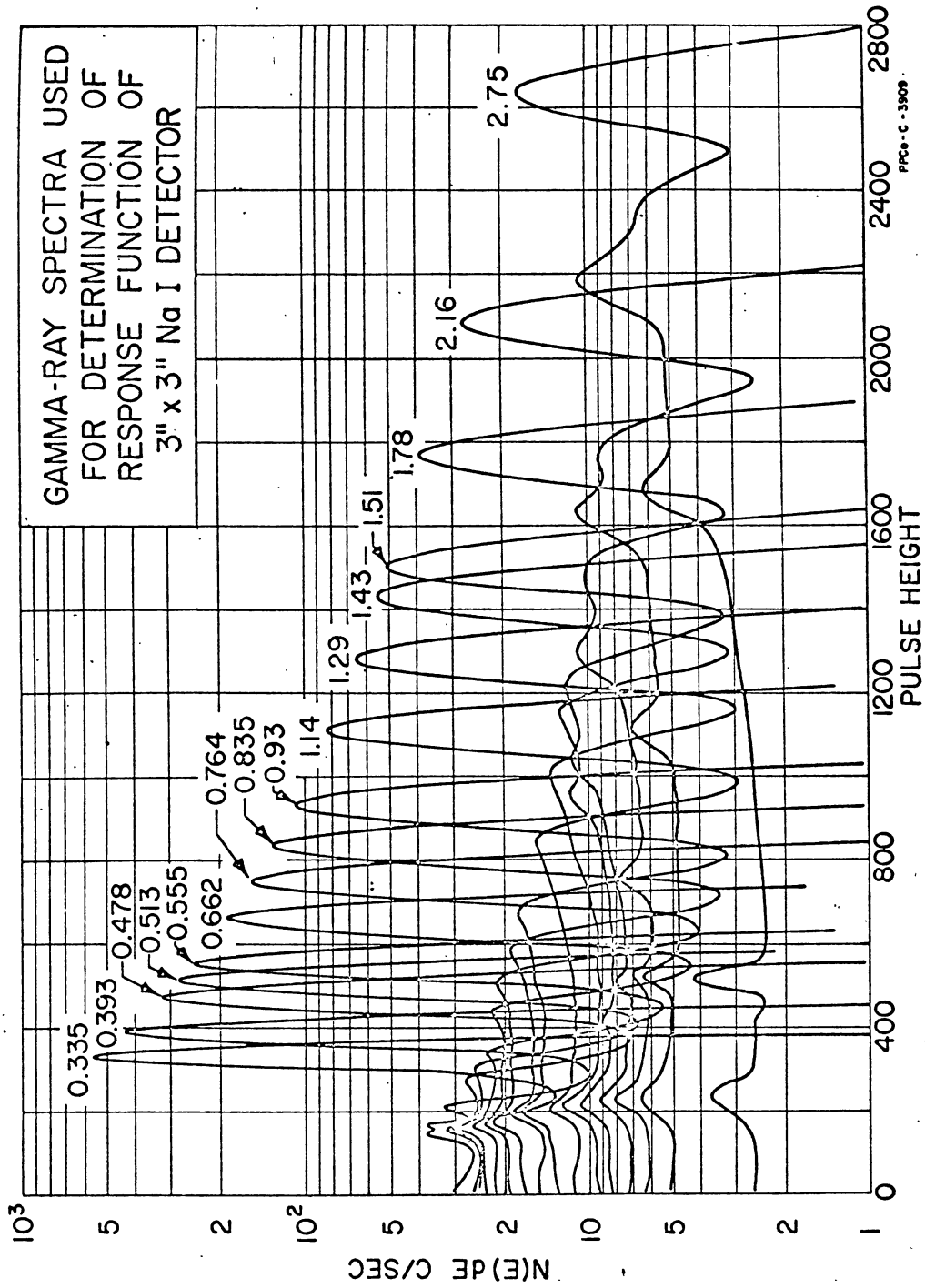

Figure 12. (Heath 1964)

$$E_b = E_\gamma - E_c = \frac{E_\gamma}{1 + 2E_\gamma/mc^2} \qquad (3)$$

Clearly, $E_b < mc^2/2$ for all E_γ, and consequently this bump will pose no problem for unfolding the pulse-height information above 300 kev.

B. Techniques for Unfolding Energy Spectra

Nuclear spectroscopists, naturally, have been active in devising schemes for the unfolding of pulse-height distributions into gamma ray intensities. Let us assume that a hypothetical radioactive source emits a series of lines given by

$$N(E_\gamma) = \sum_{i=1}^{N} a_i \, \delta(E_\gamma - E_i)$$

Then, if one knew the pulse-height distributions for mono-energetic sources of energies $E_1, E_2, \ldots, E_N$ and of unit strength, one could determine the intensities $a_1, a_2, \ldots a_N$ from a least-squares fit to the empirical data. But how does one estimate the pulse-height distribution for each of the fictitious mono-energetic gamma ray emitters?

There are two basic approaches to this problem. One technique, as reviewed by Zerby (1963), is to statistically sample, by Monte Carlo simulation, the distribution of ionization losses incurred in the appropriate metal halide crystal when it is exposed to a mono-energetic beam of gamma rays. If this method is chosen, one must follow the some-

times involved sequence of events occurring in the crystal for a large number of photons. Then, from theory or empirical data, one must convert the ionization loss distribution into a light output distribution. Finally,from estimated light collection efficiency and photomultiplier response, the pulse-height distribution is arrived at.

The alternative approach, interpolation, is perhaps less elegant but may in some circumstances be more accurate. The complete pulse-height distributions for a sequence of standard mono-energetic gamma ray sources is measured -preferably with the same instrument and under the identical conditions that will be present in the actual investigation of the unknown source. Then one interpolates between these standard curves to obtain the pulse-height distribuiton for an arbitrary mono-energetic gamma ray source. We have chosen the interpolation over the Monte Carlo method because of its simplicity and economy (of computer time). More elaborate matrix inversion techniques for unfolding spectra have been developed - in particular, for space applications by Trombka at Goddard Space Flight Center (to be published). With this extension of the interpolation procedure no assumptions need be made as to the form of the spectrum.

C. The Interpolation Method

1. The Library of Standard Pulse-Height Spectra

The interpolation technique has gradually evolved

from primitive "eyeball" judgment to the modern theory developed by Heath and his coworkers (Heath 1964, Heath et al. 1965). First, they made very careful measurements of the pulse-height distributions from a series of gamma ray sources(Figure 12). Fortunately, for our purposes, these studies were made with a 3" x 3" NaI detector. The source was located on the symmetry axis, 10cm. above the top face, and the results were normalized to 10^7 radioactive decays. Moreover, the system was adjusted so that

a. The lower limit of channel 0 corresponded to zero energy.

b. The Cs^{137} peak (.662 Mev) fell at exactly 10 kev/channel.

If x labels the channel number, the photopeak x_0 could be represented empirically by the modified Gaussian expression (Heath et al. 1965):

$$y(x) = Y_0 e^{-(x-x_0)^2/b_0}\left[1 - \alpha_1(x-x_0) + \alpha_2(x-x_0)^{12}\right] \quad (4)$$

where

$$b_0 = w_0^2 / 4(\ln 2) \quad (5a)$$

with the full width at half maximum for their instrument and electronics given by

$$w_0 = -1.4816 + 1.0085\, x_0^{1/2} - .027944\, x_0 + .0023692\, x_0^{3/2} \quad (5b)$$

The peak channel x_o is not exactly proportional to E_o the incident gamma ray energy, but rather, as a result of non-linearities in light output, is better approximated by the formula below relating pulse-height to energy loss

$$x \approx 1.320 + 97.55\ E + 3.885\ E^2 - 6.453\ E^3 + 2.841E^4 - .3894E^5 \quad (6)$$

From a least-squares fitting routine, the non-Gaussian correction terms were found to approximate

$$\log_{10}\alpha_1 = 11.536 + 11.495(\log_{10}x_o) - 5.116(\log_{10}x_o)^2 + .6488(\log_{10}x_o)^3 \quad (7a)$$

$$\log_{10}\alpha_2 = 14.652 - 31.614(\log_{10}x_o) + 14.415(\log_{10}x_o)^2 - 2.626(\log_{10}x_o)^3 \quad (7b)$$

Y_o is chosen so that the fraction of emitted gamma rays recorded under the photopeak obeys the empirical formula

$$A\varepsilon_p = 3.42\times10^{-4} + 6.84\times10^{-3}\ E^{-1} - 4.19\times10^{-4}E^{-2} + 3.8\times10^{-4}E^{-4} + 1.88\times10^{-5}E^{-5} \quad (8)$$

where A is a correction for the presence of a thin 1.18 g/cm^2 Be absorber. Then from (4), the normalization is

$$Y_o = \frac{10^7\ A\varepsilon_p}{(\pi b_o)^{\frac{1}{2}}\left[1+(3/4)\alpha_1 b_o^2+(10,395/64)\alpha_2 b_o^6\right]} \quad (9)$$

2. The Stretched Pulse-Height Distributions

The first step in the interpolation scheme is to subtract off the photopeak contribution from each mono-energetic gamma ray pulse-height spectrum.

One is then left with a set of residual Compton scattered pulse-height distributions. A naive approach would be to proceed by performing a least-squares polynomial fit to the data for each channel in powers of the peak channel. However, because of the sharp cut-off at the Compton edge, this is unsuitable. Each function would have a region where it varied rapidly and a polynomial of high degree would be required to fit the points; even if the points were fit very closely, the interpolation would be highly inaccurate unless the reference pulse-height spectra were in near proximity.

In order to circumvent this problem, a new set of residual pulse-height spectra are constructed, but expressed in terms of a variable z, the pseudo-pulse-height, rather than the true pulse-height channel x. The pseudo-pulse-height channel z is specifically defined so that the number of counts per channel (for a fixed channel) is a slowly varying function of gamma ray energy.

Depending on whether the incident energy is greater than or less than 1.3 Mev, the x-axis is broken up into segments bounded as shown in Table 4 where X_b is the channel corresponding to the back-scatter peak, X_2 the double escape peak X_1 the single escape peak, X_c the Compton edge, and X_o the

full energy peak, as determined from (1), (2), (3) and (6).

Table 4

Energy	Segment	Lower Limit	Upper Limit	Number of Equally Spaced Points
$E_o < 1.3$ Mev	1	1	X_b	51
	2	X_b	X_c	100
	3	X_c	X_o	50
$E_o < 1.3$ Mev	1	1	X_b	51
	2	X_b	X_2	50
	3	X_2	X_1	50
	4	X_1	X_c	50
	5	X_c	X_o	50

Then let z be a linear function of x in each such interval with the entire segment being mapped into a number of equal intervals on the z-axis as defined in Table 4. E.g., if $E_o < 1.3$ Mev; then $x = 1$ is mapped into $z = 1$, $x = X_o$ is mapped into $z = 52$, $x = X_c$ is mapped into $z = 151$, and $x = X_o$ is mapped into $z = 201$. Now let the nubmer of counts in each channel of this "stretched" pulse-height distribution be defined by

$$y(z(x)) = y(x)$$

for fixed energy E_o. Then the value of y(z) represents the

number of counts per unit Δx, not per unit Δz. For this reason $y(z)$ is more properly termed a pseudo-pulse-height distribution.

3. The Polynomial Fitting Procedure

We now have a set of m_1-m_2 pseudo-pulse-height distributions, m_1 obtained from sources of energy less than 1.3 Mev, and m_2 obtained from sources of energy greater than 1.3 Mev. To be precise, $m_1 = 11$, corresponding to the gamma ray emitters In-115m (.336 Mev), In - 113m (.393) Mev,Be-7 (.478 Mev), Sr-85 (.513 Mev), Y-91m (558 Mev) Cs-137 (.662 Mev), Nb-95 (.931Mev), Mn054(.835 Mev) Nb-92 (.931 Mev), Zn-65 (1.114 Mev), Ar-41 (1.29 Mev); and $m_2 = 6$ corresponding in gamma ray emitters Ar-41 (1.29 Mev), V-52 (1.43 Mev), K-42 (1.51 Mev), A1-28 (1.78 Mev), K-38 (2.16 Mev), Na-24 (2.75 Mev). It should be noted that Na-24 also radiates at 1.37 Mev. This contribution has been subtracted off by Heath (1964) and the results normalized to the emission of 10^7 of the 2.75 Mev photons.

Separately for each of the two energy ranges, we wish to make a polynomial fit, for each integral value of z to the residual stretched pulse-height distributions in powers of the peak channel. The discussion follows that in Ascher and Forsythe (1958) and Heath,et al. (1965).

For fixed z, let $f_1, f_2, \ldots, f_m$ ($m = m_1$ or m_2) be the set of stretched pulse-height data points corresponding to energies

E_1, E_2 ..., E_m and peak channels x_1, x_2, ..., x_m as calculated from (6). Let $p_i(x)$ be a polynomial of degree i. Then we wish to find coefficients S_o, S_1,..., S_n such as to minimize the function

$$Q = \sum_{k=1}^{m} \left[f_k - \sum_{i=0}^{n} S_i p_i(x_k) \right]^2 \qquad (10)$$

Setting the partial derivatives $\partial Q / \partial S_i = 0$, we have

$$\sum_{k=1}^{m} \sum_{j=o}^{n} p_i(x_k) p_j(x_k) S_j = \sum_{k=1}^{m} f_k p_i(x_k) \qquad (11)$$

Define

$$W_{ij} = \sum_{k=1}^{m} p_i(x_k) p_j(x_k) \qquad (12a)$$

$$\omega_i = \sum_{k=1}^{m} f_k p_i(x_k) \qquad (12b)$$

then (11) simplifies to

$$\sum_{j=o}^{n} W_{ij} S_j = \omega_i \qquad (13)$$

If the $p_i(x_k)$ are required to be orthogonal:

$$W_{ij} = \sum_{k=1}^{m} p_i(x_k) p_j(x_k) = 0 \qquad (i \neq j), \qquad (14)$$

then we have n equations

$$W_{ii} S_i = \omega_i \tag{15a}$$

or

$$S_i = \frac{\omega_i}{W_{ii}} = \frac{\sum_{k=1}^{m} f_k p_i(x_k)}{\sum_{k=1}^{m} \left[p_i(x_k)\right]^2} \tag{15b}$$

It only remains to construct the set of orthogonal polynomials. Let

$$p_o(x) = 1$$

Then recalling that $p_i(x)$ is a polynomial of degree i, it is obvious that one can construct higher polynomials by the rule

$$p_1(x) = x\, p_o(x) - \alpha_1 p_o(x)$$

$$p_2(x) = x\, p_1(x) - \alpha_2 p_1(x) - \beta_1 p_o(x)$$

. . . .

. . . .

. . . .

$$p_{i+1}(x) = x p_i(x) - \alpha_{1+1} p_i(x) - \beta_i p_{i-1}(x)$$

It is then straight forward to show that the orthogonality conditions (14) holds of and only if:

$$\alpha_{i+1} = \frac{\sum_{k=1}^{m} x_k \left[p_i(x_k)\right]^2}{\sum_{k=1}^{m} \left[p_i(x_k)\right]^2} \tag{16a}$$

$$\beta_i = \frac{\sum_{k=1}^{m} \left[p_i (x_k) \right]^2}{\sum_{k=1}^{m} \left[p_{i-1} (x_k) \right]^2} \qquad (16b)$$

From the above sets of equations the α_i, β_i, and p_i can all be calculated recursively. It is important to observe that the α_i and β_i, and therefore, the p_i, depend on the set of x_k. This means that the polynomials generated in this way will not, in general, be orthogonal for some other choice of input spectra.

For each value of z there are m points available for the polynomial fit. The orthogonal polynomial of degree n = m-1 would pass right through the m data points. However, as n is increased, the oscillations between points become larger and the calculation becomes less reliable as it becomes more combersome. It is, therefore, desirable to choose n to be small enough that the interpolation between points is smooth, but large enough to provide an accurate fit to the data. In the .3 - 1.3 Mev region, m = 11, n was taken to be 5; in the 1.3 - 2.75 Mev region, m = 6, n was chosen to be 3. The set of coefficients α_i, β_i, and S_i which were derived by the procedure above are displayed in the Appendix.

4. Regeneration of Spectra

With the set of orthogonal polynomials and coefficients

it is possible to calculate the residual stretched pulse-height distribution $y(z;E_o)$ for a source of any energy E_o placed on axis, 10 cm above the crystal and normalized to 10^7 decays:

$$y(z;E_o) = \sum_{i=o}^{n} S_i p_i(X_o) \qquad (17)$$

where X_o is calculated by the substitution of E_o into equation (6). It is then an easy task to reconstruct the true Compton continuum pulse-height spectrum. For each integral value of x, the corresponding value of z is found by the rule set forth in Seciton 2. In general, that value of z will not be an integer: suppose it lies between the integers z_1 and z_2. Then through interpolation of the results for $y(z_1;E_o)$ and $y(z_2;E_o)$ from equation (17), one can get $y(x(z); E_o)$.

Finally, the full energy peak is calculated from equations (4)-(9) and added in to yield the complete pulse-height distribution for a source of energy E_o. As a test of the entire procedure, we regenerated the input spectra provided by Heath and found, after small adjustments in the positions of the peaks made necessary by round-off errors, that the spectra were duplicated to a precision:

$$\frac{\left(\sum |y(x_i) - y'(x_i)|^2\right)^{\frac{1}{2}}}{\sum y(x_i)} < 1\% \qquad (18)$$

where $y(x_i)$ and $y'(x_i)$ are the number of counts in channel x_i according to the input and regenerated spectrum, respectively, and where the summations go over all channels.

D. The Angular Response of a Cylindrical Detector

In astrophysical experiments an uncollimated NaI crystal is exposed to gamma rays incident from all directions. If the flux is isotropic, of intensity $I cm^{-2} sec^{-1}$, and the detector is 100% efficient, the omnidirectional geometry factor of the detector G_o is defined by

$$C = G_o I \tag{19}$$

where C is the counting rate. For a cylindrical detector of radius r and thickness h,

$$G_o = \int_0^1 \pi r^2 \mu d\mu + \int_0^1 2rh(1-\mu^2)^{\frac{1}{2}} d\mu \tag{20}$$

where μ is the direction cosine between the angle of incidence and the symmetry axis. Solving by quadratures:

$$G_o = \tfrac{1}{2}\pi r^2 + \tfrac{1}{2}\pi rh \tag{21}$$

For the interesting case where h = 2r,

$$G_o = 3/2\ \pi r^2 \tag{22}$$

Implicit in the following, unless otherwise stated, is that h = 2r = 3".

In the real world low energy gamma ray detectors are not 100% efficient. If one considers a broad parallel beam of radiation at some angle θ with respect to the crystal axis (for the remainder of this discussion the symmetry axis is also the polar axis and the zenith direction), the efficiency is going

to depend in some way on the ratio of the absorption length for a gamma ray in NaI to some average thickness of material encountered by the beam in traversing the detector. The absorption length, of course, varies with energy; moreover, the shape of the angular response curve describing the detector also varies with energy. A simple example will illustrate this latter point.

Suppose first, that the absorption length λ is much smaller than the dimensions of the crystal. Then the efficiency η will be nearly unity in any direction. The area x efficiency factor at $\theta = 0^o$ is

$$(A\eta)_{\theta = 0^o} = \pi r^2$$

at $\theta = 90^o$,

$$(An)_{\theta = 90^o} = 2rh = 4r^2$$

I.e., for $\lambda << r$,

$$\frac{(An)_{\theta=0}}{(An)_{\theta=\pi/2}} = \pi/4 \qquad (23)$$

If, on the other hand, $\lambda >> r$, the efficiency is just δ/λ where δ is the thickness of material through which the gamma rays pass. At $\theta = 0$,

$$(An)_{\theta=0} = \pi r^2 (2r/\lambda)$$

At $\theta = \pi/2$, define a set of rectangular coordinates with the beam direction parallel to the x-axis and the z-axis coincident with the crystal axis, then

$$(An)_{\theta = \pi/2} = 2r \int_{-r}^{r} dy\, 2(r^2 - y^2)^{\frac{1}{2}}/\lambda$$

Making the substitution $y = r \sin \phi$

$$(An)_{\theta = \pi/2} = \frac{4r^3}{\lambda} \int_0^{\pi} \cos^2 \phi \, d\phi$$

$$= (4r^3/\lambda)\ (\pi/2)$$

I.e., for $\lambda >> r$,

$$\frac{(An)_{\theta=0}}{(An)_{\theta=\pi/2}} = 1 \qquad (24)$$

A comparison of (23) and (24) makes it apparent that the efficiency does not change uniformly with energy as the direction of the incident beam is altered.

1. The Effective Area - Efficiency of a Thin Slab

Suppose we have a uniform parallel beam of monenergetic gamma rays at an angle θ with respect to the symmetry axis of the detector. As in the above discussion, define the coordinate system with the z - axis perpendicular to the crystal faces and oriented so that the photons have no y-component to their momenta. Thanks to the cylindrical symmetry of the problem, it will suffice to find the area-efficiency factor, as a function of θ, for this orientation in order to completely specify the angular response.

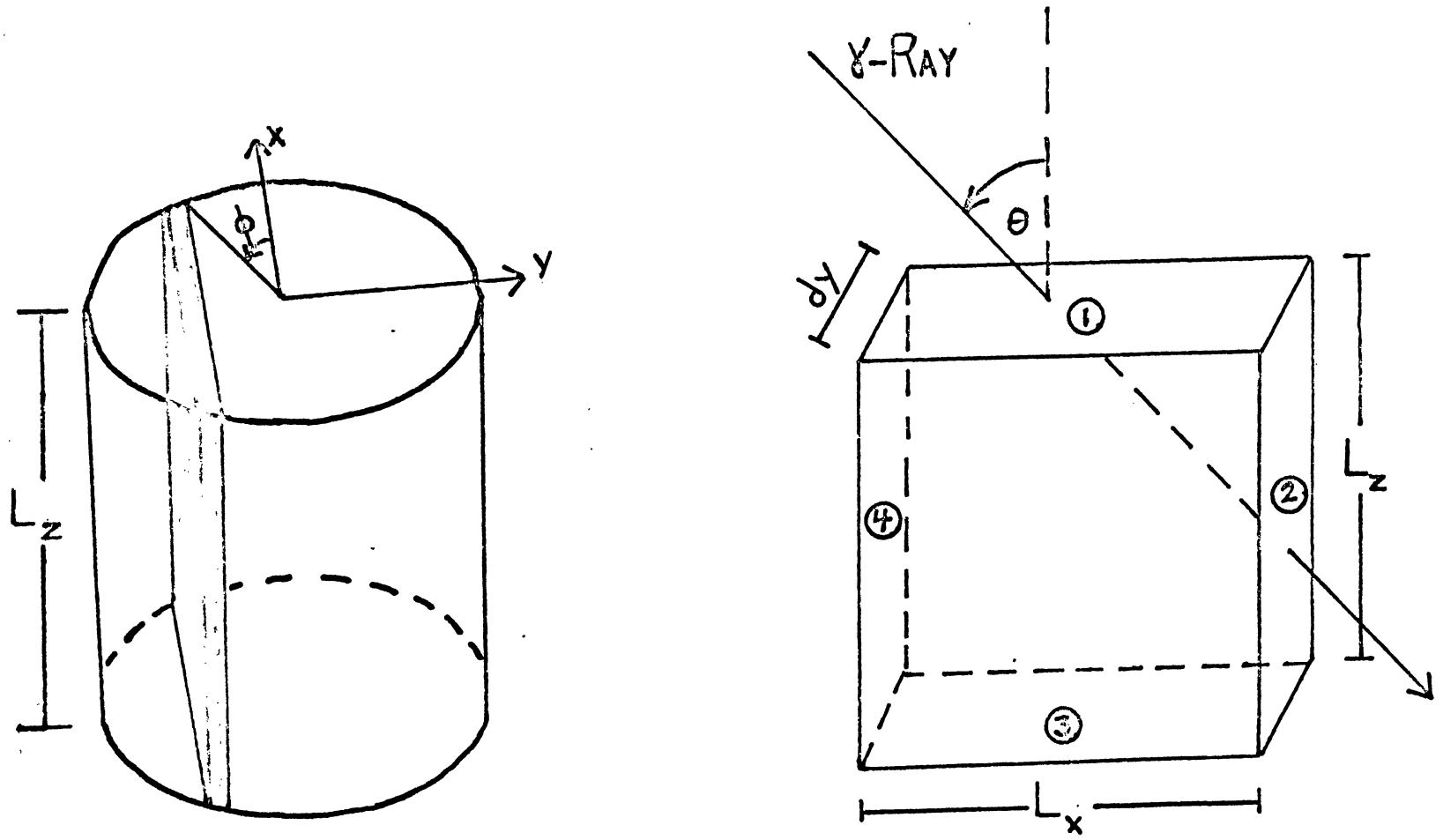

Figure 13. Crystal Cut Into Thin Slabs

Now imagine that the crystal is cut along the x direction, from the top face through to the bottom face, into a large number of thin slices, each of thickness dy. If dy is made sufficiently small, each slice is nearly a rectangular parallelepiped of length $L_x = 2r \cos \phi$, width dy, and height $L_z = h = 2r$, where $\cos \phi$ is the cosine of the angle between the radius vector drawn to an infinitesmal side dy and the x-axis (see Figure 13). Number the faces of constant x and constant z sequentially for each slice, starting with the top face and proceeding clockwise about the y - axis; i.e., the faces are named as follows:

Table 5

Number	Face
1	$z = 0$
2	$x = L_x$
3	$z = L_z$
4	$x = 0$

Consider the radiation incident on an isolated slice. Since there is no y - component of momentum, a photon passing through the parallelepiped can trace only one of four possible courses: enter face #1, exit face #3; enter #1, exit #2; enter #4, exit #2; enter #4, exit #3. Some of these routes may be impossible; e.g., if $\theta = 0^o$, all the radiation passing directly through the crystal will enter #1 and exit #3. The im-

portant parameters for each path, for an arbitrary slice and zenith angle, are tabulated below:

Table 6

Path	Path Length	Element of Area	Limits of Integration
$1 \rightarrow 3$	$L_z/\cos\theta$	$\cos\theta \; dxdy$	$x = 0,\ t(L_x - L_z \tan\theta)$
$1 \rightarrow 2$	$(L_x - x)/\sin\theta$	$\cos\theta \; dxdy$	$x = t(L_x - L_z\tan\theta), L_x$
$4 \rightarrow 2$	$L_x/\sin\theta$	$\sin\theta \; dzdy$	$z = 0,\ t(L_z - L_x/\tan\theta)$
$4 \rightarrow 3$	$(L_z - z)/\cos\theta$	$\sin\theta \; dzdy$	$z = t(L_z - L_x/\tan\theta),\ L_z$

where $t(\xi)$ means the maximum of either ξ or zero. The first column notes a pair of entrance and exit faces through which a photon may pass into and out of the slice. The second column records the total path-length of such a photon in the slab. This may be a function of the x or z coordinate on the entrrnce face where the photon strikes the slab. In column 3 the elements of area, normal to the photon beam, on the entrance face are indicated. In column 4, the limits of integration over the narrow entrance face are listed with proper allowance being made for the correct exit face.

Let J_o be the intensity of the parallel monochromatic beam and let C_{ij} be the number of quanta/second that enter face i and leave face j. Then if the absorption length in NaI at this energy is λ it follows from Table 6 that

$$C_{13} = J_o \, dy \cos\theta \int_0^{t(L_x - L_z \tan\theta)} dx \, e^{-L_z/\lambda \cos\theta} \tag{25a}$$

$$C_{12} = J_o \, dy \cos\theta \int_{t(L_x - L_z \tan\theta)}^{L_x} dx \, e^{-(L_x - x)/\lambda \sin\theta} \tag{25b}$$

$$C_{42} = J_o dy \sin\theta \int_0^{t(L_z - L_x/\tan\theta)} dz \, e^{-L_x/\lambda \sin\theta} \tag{25c}$$

$$C_{43} = J_o dy \sin\theta \int_{t(L_z - L_x/\tan\theta)}^{L_z} dz \, e^{-(L_z - z)/\lambda \cos\theta} \tag{25d}$$

For $L_x > L_z \tan\theta$:

$$C_{13} = J_o dy \cos\theta \, (L_x - L_z \tan\theta) \, e^{-L_z/\lambda \cos\theta} \tag{26a}$$

$$C_{12} = J_o dy \, \lambda \sin\theta \cos\theta \, (1 - e^{-L_z/\lambda \cos\theta}) \tag{26b}$$

$$C_{42} = 0 \tag{26c}$$

$$C_{43} = J_o dy \lambda \sin\theta \cos\theta \, (1 - e^{-L_z/\lambda \cos\theta}) \tag{26d}$$

For $L_x < L_z \tan\theta$:

$$C_{13} = 0 \tag{27a}$$

$$C_{12} = J_o dy \lambda \sin\theta \cos\theta \, (1 - e^{-L_x/\lambda \sin\theta}) \tag{27b}$$

$$C_{42} = J_o dy \sin\theta \, (L_z - L_x/\tan\theta) e^{-L_x/\lambda \sin\theta} \tag{27c}$$

$$C_{43} = J_o dy\, \lambda \sin\theta \cos\theta \left(1-e^{-L_x/\lambda \sin\theta}\right) \qquad (27d)$$

Let C' be the number of photons transmitted through the slice per second. Then,

$$C' = C_{13} + C_{12} + C_{42} + C_{43} \qquad (28)$$

Then from (26), (27), (28) and some algebra

$$C' = J_o dy \left[2\lambda \sin\theta\cos\theta + e^{-L_z/\lambda\cos\theta}\left(L_x\cos\theta - L_z\sin\theta - 2\lambda\sin\theta\cos\theta\right)\right] \quad (L_x > L_z\tan\theta) \qquad (29a)$$

$$C' = J_o dy \left[2\lambda \sin\theta\cos\theta + e^{-L_x/\lambda\sin\theta}\left(L_z\sin\theta - L_x\cos\theta - 2\lambda\sin\theta\cos\theta\right)\right] \quad (L_x < L_z\tan\theta) \qquad (29b)$$

A check on the calculation to this point is the necessary symmetry of the above expressions:

$$(29a) \longleftrightarrow (29b)$$

$$(L_x,\ L_z,\ \sin\theta\ ,\ \cos\theta) \longleftrightarrow (L_z,\ L_x,\ \cos\theta\ ,\ \sin\theta)$$

The area-efficiency factor of the slab is now completely specified. For energy E, it is given by

$$A_s(\theta) \times \left[1-\eta_s(E,\theta)\right] = C'(\lambda(E))/J_o \qquad (30)$$

where the area factor,

$$A_s(\theta) = L_x dy \cos\theta + L_z dy \sin\theta \qquad (31)$$

and η_s (E, θ) is by definition the angular efficiency of the slice at energy E.

2. The Area - Efficiency Factor for a Cylindrical Crystal

To get the angular response of the whole crystal, we must integrate equation (30) over all the slices with C' substituted from (29a,b). If A(θ) and $\eta(E,\theta)$ are the area and efficiency of the detector as a function of zenith angle and energy, then

$$A(\theta)\ [1-\eta(E,\theta)] = 2/J_o \int_o^r dy\ C'(y) \tag{32}$$

C' can be expressed as a function of y by recalling that

$$L_x = 2r\cos\phi = 2(r^2-y^2)^{\frac{1}{2}} \tag{33}$$

and that

$$L_z = 2r \tag{34}$$

Substituting (33) and (34) into (29) and the resulting expression into (32), we have

$$A(\theta)\ [1-\eta(E,\theta)] = 4\lambda r \sin\theta\cos\theta + 4\int_o^{y^*} dy\ e^{-2r/\lambda\cos\theta}\left[(r^2-y^2)^{\frac{1}{2}}\cos\theta - r\sin\theta - \lambda\sin\theta\cos\theta\right] + 4\int_{y^*}^{r} dy \left\{ e^{-2(r^2-y^2)^{\frac{1}{2}}/\lambda\sin\theta}\left[r\sin\theta-(r^2-y^2)^{\frac{1}{2}}\cos\theta - \lambda\sin\theta\cos\theta\right]\right\} \tag{35}$$

where y^* is defined by equations (19a,b) to be the value of y, between 0 and r, when

$$L_x = L_z \tan \theta \tag{36}$$

or from (33) and (34),

$$4(r^2 - y^{*2}) = 4r^2 \tan^2 \theta$$

solving for y^*

$$y^* = r(1-\tan^2\theta)^{\frac{1}{2}}$$

Sometimes equation (36) will lead to non-physical values for y^*. The full definition of y^* is written below.

$$\begin{aligned} y^* &= r(1-\tan^2\theta)^{\frac{1}{2}} && (0^o<\theta<45^o) \\ y^* &= 0 && (45^o<\theta<90^o) \end{aligned} \tag{37}$$

The first integral on the right of equation(35) can be done analytically, so that

$$A(0)\left[1-\eta(E,\theta)\right] = 4\lambda r \sin\theta \cos\theta + 4e^{-2r/\lambda\cos\theta}$$

$$\tfrac{1}{2}r^2\cos\theta(\alpha^* + \tfrac{1}{2}\sin 2\alpha^*) - y^* \sin\theta(r+\lambda\cos\theta) + 4\int_{y^*}^{r} dy \ldots \tag{38}$$

where

$$\alpha^* = \sin^{-1}(y^*/r) \tag{39}$$

The second integral in equation (35) can be evaluated numerically. Then the area-efficiency factor is easily arrived at by noting:

$$A(\theta)\ \eta\ (E,\theta) = A(\theta) - A(\theta)\ \left[1-\eta\ (E,\theta)\right] \tag{40}$$

where the effective area of the entire crystal is given by

$$A(\theta) = \pi r^2 \cos\theta + 2rh \sin\theta \qquad (41)$$

The curves in Figure 14 indicate the results of the calculation, for several energies, for a 3" x 3" NaI cylindrical detector.

Also displayed on the graph are experimental data points which we obtained in the preliminary calibration of the 3" x 3" NaI detector described in Chapter III. For these studies a gamma ray source was located 20" from the geometric center of the crystal. The output pulses were sent from the photomultiplier to a 100 channel pulse-height analyzer, manufactured by Technical Measurment Corporation (Model 102), where they were placed into pulse-height bins and counted. The pulse-height distributions were recorded separately, for equal time intervals, with the source placed at 0^o, 30^o, 45^o, 60^o and 90^o with respect to the crystal axis. In Figure 14, the angular variation of the area under the full-energy peak, as a function of energy and angle, are plotted. For the sake of comparison, the results at each energy are normalized to match the theoretical area-efficiency curve at $\theta = 0^o$.

Although the distance from the source to the center of the crystal was constant to 1%, the average intensity irradiating the surface of the detector varies somewhat with the angular position of the emitter. We have estimated and

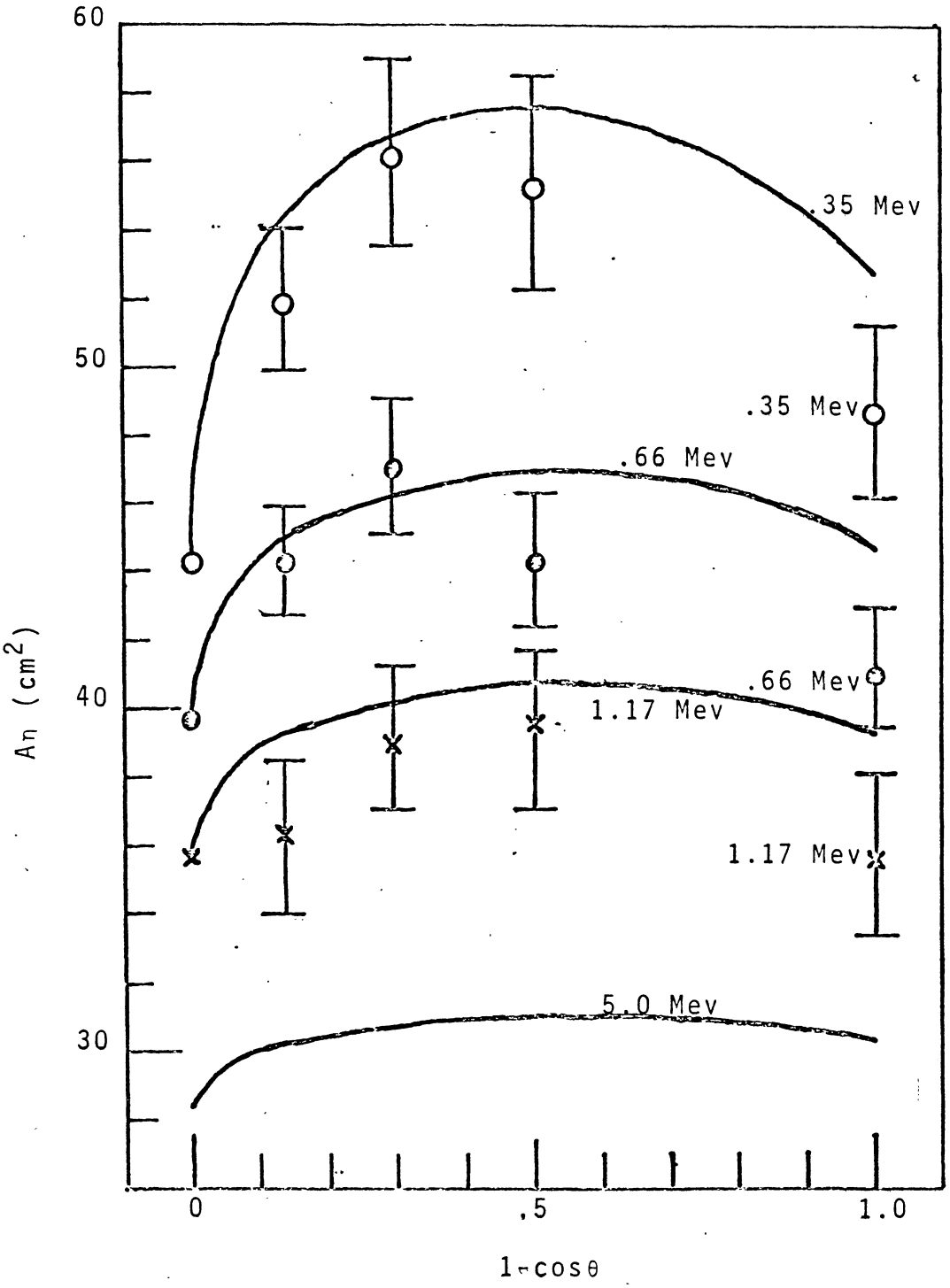

Fig. 14. Area - Efficiency of 3" x 3" NaI Crystal.

corrected for this and for the scattering in the surrounding material. The error bars in Figure 14 include remaining uncertainty in those factors, in the position of the source, as well as statistical fluctuations in the number of counts.

In spite of the approximation to a parallel uniform flux by a point source (the angle of incidence was typically defined to a 6^{o} half-angle), the agreement with the shape of the theoretical curve is quite good when $\theta \leq 45^{o}$. There is strong disagreement at 90^{o}, where it appears that the fraction of counts contained in the full energy peak, i.e., the peak-to-total ratio, is anomolously low. The same effect has been observed by Trombka (to be published). The reduction in the peak-to-total ratio corresponds to the increased probability for escape after a small angle scattering.

3. The Response of the Detector to an Isotropic Flux

Taking the calculations of the previous section one step further, we can evaluate the integrated isotropic area-efficiency factor of the detector, as a function of energy. Defining $\mu = \cos\theta$ and noting that

$$\sin\theta = (1-\mu^{2})^{\frac{1}{2}},$$

$$1-\tan^{2}\theta = 2 - \mu^{-2},$$

theta can be eliminated in favor of mu in equation (38). Then multiplying both sides by the equal solid angle factor $d\mu$ and integrating from 0 to 1, we can solve for the isotropic area-efficiency factor as a function of λ by using the relationship

$$A_o \eta_o(E) = A_o - A_o [1 - \eta_o(E)] \quad (42a)$$

where, as computed by (21) or (22),

$$A_o = G_o = 3/2\ \pi r^2 \quad (42b)$$

The energy dependence appears only in λ, the absorption length. In Figure 15, τ ($=1/\lambda$) is plotted versus energy for NaI. An analytical representation of that curve, as obtained by a fitting program, is:

$$\ln\tau = 1.516 - .2941(\ln E) + .4104\ (\ln E)^2 \quad (.26<E<1\ \text{Mev}) \quad (43a)$$

$$\ln\tau = -1.512 - .6604(\ln E) + .1991\ (\ln E)^2 \quad (1<E<10\ \text{Mev}) \quad (43b)$$

It is convenient to introduce a quantity R_o, defined by

$$R_o = \frac{\eta_o}{\eta(0)} \quad (44)$$

where η_o is the efficiency, averaged over solid angle for an isotropic flux, as defined by (42); $\eta(0)$ is the efficiency of detection at $\theta = 0^o$:

$$\eta(0) = 1 - e^{-\tau h} \quad (45)$$

The energy labelling has been suppressed.

R_o was computed for a large number of values of tau from equations (35) - (42), (44) and (45). A least squares fit yielded the formula of (46), applicable to a 3" x 3" NaI detector,

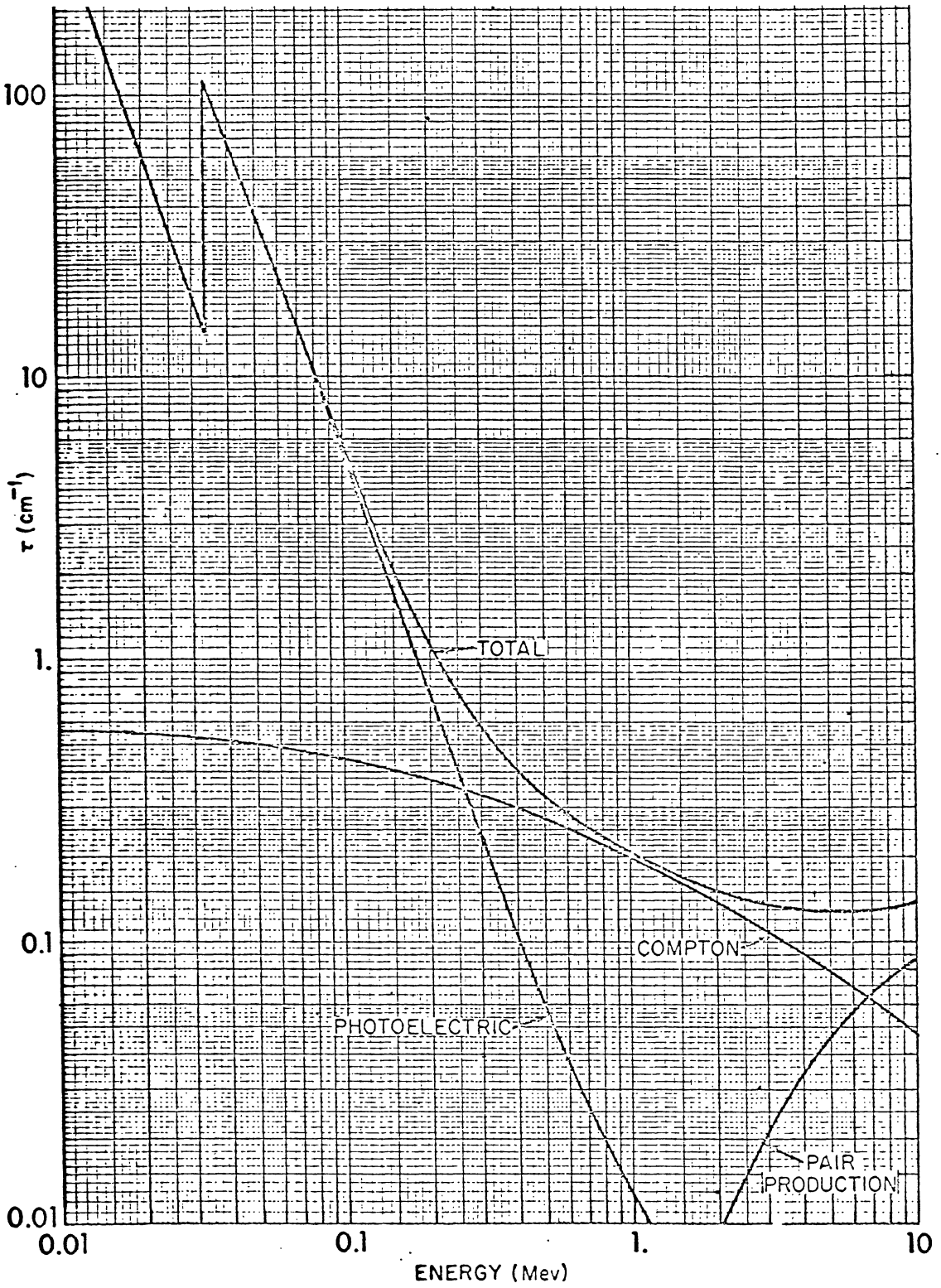

Figure 15, (Nat. Bureau of Standards Circular NBS - 583, 1962)

$$R_o = .6609 + .48815\,\tau - .2433\,\tau^2 \qquad (E > .22 \text{ Mev}) \qquad (46)$$

to 1% precision, where tau is given by Figure 15 or equations (43 a,b). In the low energy limit, both η_o and $\eta(0)$ approach unity, consequently,

$$R_o = 1 \qquad (\tau r >> 1) \qquad (47)$$

As the attenuation length is increased, it is apparent from Figure 14 that the response of the crystal approaches isotropy, that is,

$$\eta(0)A(0) = \eta(\theta)A(\theta) \qquad (\tau r << 1) \qquad (48)$$

for all theta. Integrating both sides of equation (48) over solid angle, we have with the help of (41),

$$\eta_o\, 3/2\pi r^2 = \eta(0)\pi r^2$$

or

$$R_o = 2/3 \qquad (\tau r << 1) \qquad (49)$$

Equation (46) can be used for any 3" x 3" cylindrical detector. The results must, however, be interpreted in the light of the appropriate tau versus E dependence for the particular detector substance. E.G., if the correct energy dependence is allowed for, the expression is valid for a 3" x 3" CsI detector when E> .28Mev.

We can generalize the above results still further, to any h x h cylindrical detector, by noting that R_o can be expressed as a function of the ratio λ/h or τh. Writing (46)

in the invariant form

$$R_o = .6609 + .06406\ \tau h - .004190\ (\tau h)^2 , \qquad (50)$$

we have an expression for R_o applicable to any cylindrical detector of thickness h, diameter h = 2r, independent of h or material, in the energy range defined by

$$\tau(E)h < 7$$

Moreover, it is clear that the limiting expressions, (47) and (49), apply to any such detector.

CHAPTER V

EXPERIMENTAL PREDICTIONS

A. The Energy Loss Spectrum in the .3-2 Mev Range

The atmospheric background flux at 3.5 g/cm^2, 40^o latitude has been explored by Peterson and Schwartz (private communication) with an uncollimated 3" x 3" NaI detector. Their measurements are summarized in Figure 16 - the data is presented in counts/cm^2 sec Mev, with no attempt being made to unfold the gamma ray spectrum. But the equations of the last chapter allow an estimation of the response of such an instrument to an arbitrary low energy gamma ray flux. This enables us to check the calcualtions in Chapter II by using them to predict what should be observed with a 3" x 3" NaI detector at 3.5 mb and then comparing them with the results of Peterson and Schwartz.

The library of standard sources of Chapter IV included gamma ray emitters only up to 2.75 Mev, so that even with reasonable extrapolation, the polynomial fitting routine cannot be employed beyond E≈3 Mev. Since the pulse-height distribution below the double escape peak ($x<X_2$) is relatively flat and smoothly varying with incident energy, it is possible to estimate the number of counts in a particular channel x resulting from incident gamma rays above 3 Mev, where x<200

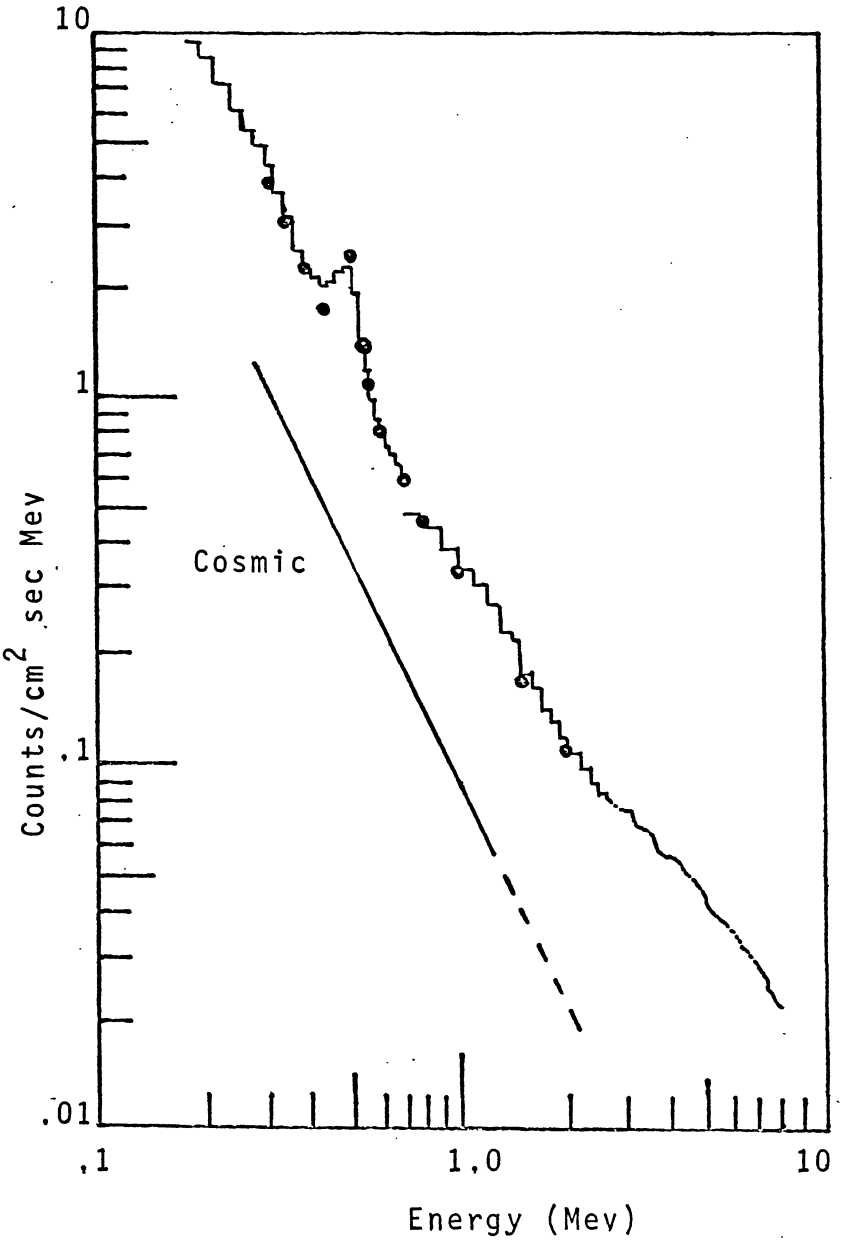

Figure 16. Atmospheric Flux at 3.5 mb (Peterson 1969).
● Calculated Count Rate.

(recall that this corresponds to <2 Mev deposited in the crystal). The correction becomes large and difficult to assess for x> 200, consequently we shall limit ourselves to the region $30 < x < 200$.

A continuum flux, like the one of Figure 11, can be approximated by a sum of monochromatic sources. If the energy range from .27 Mev to 3 Mev (to find the number of counts at x=30, photons slightly below .3 Mev must be included - their intensity in the atmosphere was obtained by extrapolation) is broken up into small intervals ΔE_i each centered about an Energy E_i, then an equivalent monochromatic flux in the i^{th} interval can be defined by the expression

$$I(E_i) = J(E_i)\ \Delta E_i \qquad (1)$$

where $J(E_i)$ = # photons/cm^2 sec Mev at $E_\gamma = E_i$.

For E_i <3 Mev, the polynomial method enables one to calculate the resulting pulse-height distribution were the crystal to be exposed to 10^7 gamma ray emissions from a monochromatic point source of energy E_i, located on-axis, 10 centimeters above the top surface. In particular, the number of counts under the full-energy peak will be given by

$$N_p = 10^7\ A\varepsilon_p \qquad (2)$$

where $A\varepsilon_p$ is found from (IV-8) evaluated at $E=E_i$. N_p is related to the total number of detected events N by the relationship

$$N_p = f_p(E_i)\, N \tag{3}$$

where $f_p(E_i)$ is the peak-to-total ratio. An analytical representation of empirical data, obtained by Heath (1964) with a series of sources placed in the above standard configuration with respect to a 3" x 3" NaI detector, is

$$f_p(E) = .424 - .628(\log_{10}E) + .388(\log_{10}E)^2 \tag{4}$$

in the energy region ($.27 < E < 3$ Mev).

Now in order to compute the pulse-height distribution from the equivalent monochromatic source of equation (1) let us make the following simplifying assumptions:

(a) The shape of the distribution will be identical to the one resulting from a point source of the same energy placed in the standard configuration. In particular, neglect the variation of $f_p(E_i)$ with the angle of incidence. Since the average (over solid angle) peak-to-total ratio may be 5-10% lower than the value at 0^o, this assumption may lead to a slightly flattened pulse-height spectrum.

(b) The number of counts per second in the full-energy peak is given by

$$dN'_p/dt = I(E_i)R_o(E_i)\ 1.5\pi r^2\ f_p(E_i)\ \eta(0;E_i) \tag{5}$$

with $I(E_i)$ given by (1), $R_o(E_i)$ by (IV-46), $f_p(E_i)$ by (3), and the efficiency at 0^o $\eta(0;E_i)$ by equations

(IV-45) and (IV-43).

In other words, first we calculate the pulse-height distribution for a standard source, normalized to (2); then we scale the entire distribution by a factor determined by (1) and (5). This renormalization is equivalent to taking the isotropic area-efficiency factor and the 0^{o} peak-to-total ratio as a description of the crystal response. Since the dominant (upward) photon intensity is nearly isotropic (Figure 5) and the response of the crystal is also a weakly varying function of angle (Figure 14), the error introduced by this assumption is expected to be <10% aside from the small distortion in shape that was mentioned above.

The pulse-height distribution at 3.5 can now be calculated in four steps.

1. The Atmospheric Continuum

Sum up the contributions, normalized to equation (5), of the equivalent line spectrum of equation (1), where $J(E_i)$ is the bremstrahlung plus scattered annihilation continuum of Figure 11. The intervals were made sufficiently narrow so as to smooth out any discontinuities - throughout the integration, ΔE_i was less than .002 E_i.

2. The .511 Mev Line

Add in the pulse-height spectrum from a monochromatic .511 Mev isotropic flux of a strength given by (II-22).

Again, the normalization is fixed by equation (5), where $I(.511\ \text{Mev}) = .20\ \text{cm}^{-2}\text{sec}^{-1}$.

3. Gamma Rays Above 3 Mev

The count rate in channel x due to these photons can be written formally as

$$C(x) = 1.5\pi r^2 \int_3^\infty dE_\gamma\ J(E_\gamma)\ g(E_\gamma, x) \qquad (6)$$

where $g(E_\gamma, x)$ is the probability that a photon of energy E_γ, upon striking the crystal, will cause a count to be registered in channel x. The probability of pair production (vis á vis Compton scattering) in NaI increases sharply as the incident energy is raised above 3 Mev. Correspondingly, a larger fraction of the events will fall in channels $x < X_2$. Moreover, the counts falling below the double escape peak will be distributed over a greater number of channels. For these reasons $g(E_\gamma, x)$ is a decreasing function of E (> 3 Mev) for x less than 200. Coupled with the monotonic decrease in $J(E_\gamma)$ with energy, it becomes possible to replace the upper limit of integration in equation (6) by $E_{max} \approx 7$ Mev.

From an extrapolation of the standard pulse-height spectra obtained by Heath, we can estimate $g(E_\gamma, x)$; $J(E_\gamma)$ is gotten from Figure 11. Recalling that each channel is $\approx$10 kev wide, one finds a pulse-height contribution from photons above 3 Mev of

$$dC/dAdE = (2.5\pm1)x10^{-2}cm^{-2}sec^{-1}Mev^{-1} \qquad (x < 200) \qquad (7)$$

where

$$E = .01\ x$$

It will turn out that this correction is negligible for $x < 100$ and less than 25% at $x = 200$.

4. Primary Gamma Rays

Finally, we must include the counts resulting from primary gamma rays arriving from outside the Earth's atmosphere. As mentioned in the introduction, Metzger et al.(1964) have investigated the diffuse flux of gamma rays in space. In the .3 to 1 Mev region, they recorded an omnidirectional energy loss spectrum given approximately by

$$dC/dAdE = .18E^{-2}\text{counts } cm^{-2}sec^{-1}Mev^{-1} \qquad (8)$$

They had a 2.75" x 2.75" CsI detector with an average mass of $2.5g/cm^2$ surrounding the instrument. It should be noted that equation (8) is not the gamma ray spectrum - an unfolding of the instrument's energy response would leave a less steep power law.

Since the behavior of a 2.75" x 2.75" CsI crystal is not very different from a 3" x 3" NaI detector and since there is not much difference in gamma ray absorption, the primary flux at 3.5 mb, over the downward hemisphere, will increase the rate by approximately

$$dC/dAdE = .09\ E^{-2}cm^{-2}sec^{-1}Mev^{-1} \qquad (9)$$

Combining all four of the contributions listed above, we arrive at the predicted pulse-height spectrum from 300 kev to 2 Mev for an uncollimated 3" x 3" NaI detector at 3.5 mb altitude and medium latitude. Some representative points are plotted along with data of Peterson and Schwartz in Figure 16. The agreement in slope and normalization is quite good. The continuum energy loss spectrum follows a power law given by

$$dC/dAdE \approx .3E^{-2.25}\,cm^{-2}\,sec^{-1}\,Mev^{-1} \qquad (10)$$

It is interesting to compare this with the bremstrahlung spectrum before the crystal response was folded in. From Figure 11 we see that the exponent in the power law describing the atmospherically produced photon flux is about -1.5 in the same energy region. So the crystal response distorts the spectrum appreciably.

By analogy, one is let to the conclusion that the cosmic diffuse flux is better described by a power law with an exponent of $\approx$ -1.4 than by the expression on the right of equation (8).

A further point for discussion is the abrupt flattening of the diffuse photon flux above 1 Mev that was recorded on the Ranger 3 flight (Arnold et al. 1962). The results from Ranger 5 call this observation into question (Metzger et al. 1964). Moreover, a flattening as large as first reported is in apparent contradiction with the measurements of Peterson

and Schwartz made near the top of the atmosphere (Figure 16). For the purposes of our calculation, we have simply extrapolated the space flux curve from 1 Mev to 2 Mev.

A more moderate flattening at about 2 Mev has been recently reported by Vette et al. (1969). If the flattening turns out to be real, it will be difficult to invent a mechanism for generating such a discontinuity in the spectrum in the 1 Mev region. There would instead have to be some distortion of the spectrum taking place during the passage of the photons through space.

One possibility for the excess would be a cosmological red-shift of higher energy photons, e.g., π^o-decay gamma rays or nuclear line emissions into the Mev region. Alternatively, it may reflect a distortion of the spectrum in passage through matter. Let us assume a photon is scattered, with an energy loss from E to E'. That particular scattering would tend to steepen the spectrum below E and flatten it above E. At a particular energy, it is not obvious whether the overall integrated effect will be one of steepening or flattening, - it will depend on the slopt of the photon spectrum and the rate of change of the cross section(Figure 15) at that energy. But it is interesting to note in this regard that a gentle flattening in the 1 Mev region can be seen in Figure 6 for upward moving atmospheric bremstrahlung. If this suggestion for the

flattening of the cosmic flux is correct, it indicates that the photons have passed thorugh a sizable amount of material before being detected. Finally, it should be noted that the crystal efficiency begins to level off in this energy region (Figure 15) - this too could give rise to an anomolous flattening.

An accurate determination of the energy spectrum for the cosmic diffuse flux is necessary before their origin can be understood. As the above discussion indicates, the theoretical energy dependence may be sensitive to the choice of cosmological model.

B. The 6.13 Mev Line

The intensity of the 6.1 Mev O^{16} line at balloon altitude was earlier found to be

$$I(6.1\ \text{Mev}) \simeq 6.4\times10^{-3}\,\text{cm}^{-2}\,\text{sec}^{-1} \qquad \text{(II-27a)}$$

This corresponds to a count rate under the full-energy peak of

$$C(6.1\ \text{Mev}) \approx 6.4\times10^{-3}\,\text{cm}^{-2}\,\text{sec}^{-1}\ (1.5\pi r^2)\ \eta_o f_p \qquad (11)$$

where r is the radius of the crystal, η_o is the isotropic efficiency, and f_p is the peak-to-total ratio. From an extrapolation of equation (3) and a consideration of the discussion at the end of the last chapter, $\eta_o f_p \simeq .07$.

This gives a count rate of

$$C(6.1\ \text{Mev}) \approx 2.75\times10^{-2}\,\text{sec}^{-1} \qquad (12)$$

On the other hand, further measurements by Peterson and

Schwartz in this energy region indicate a continuum energy loss spectrum:

$$dC'/dAdE \approx 3x10^{-2} cm^{-2} sec^{-1} Mev^{-1}$$

If the energy resolution of the instrument at 6 Mev is taken to be $\approx$3%, then there will be $\approx$.4 counts/second under the full energy peak. The line should stand out as a three deviation excess in about 100 minutes of observation time. Good resolution and especially stable gain will be necessary to confirm this flux.

C. Conclusions

From Figure 5 it appears that it is possible to study the diffuse cosmic photon flux with balloon borne collimated detectors. But in order to reduce the atmospheric background to a level 10 times less than the cosmic flux, one needs to reduce the upward and sideward flux by about a factor of 30. As discussed by Chupp (1966), the neutron induced gamma ray background in the detector and the surrounding material then becomes comparable. Morevoer, the collimation material can actually increase this component of background. Thick plastic scintillation shields, sensitive to low energy proton knock-ons, can provide some degree of rejection agains neutron events.

In any case, since the downward electron intensity is nearly constant in the first few grams of atmosphere, the downward atmospheric photon background at high altitudes should

almost a linear function of depth. The upward gamma ray albedo will be nearly constant at small depths. This allows an extrapolation to yield the atmospheric contamination; and by subtraction, the residual (primary) component. Certainly, even with only a factor of five reduction in background, a few per cent anisotropy in the diffuse flux should be detectable.

Another point to be made from Figure 5 or Figure 16 is that the atmospheric background is less than an order of magnitude greater than the diffuse space flux at balloon altitude. Consequently, the only significant gain in launching a point source detector into space is the opportunity for long observing times.

APPENDIX I

PARTICLE FLUXES

If N_β represents the number of particles of type β, then in the notation of the text, we can define the fluxes of particle β by the derivatives listed below.

$I_\beta = dN_\beta/dAdt$ (#/cm^{2}sec)

$i_\beta = dN_\beta/dA\,d\,dt$ (#/cm^{2}sec sr)

$J_\beta = dN_\beta/dAdEdt$ (#/cm^2 sec Mev)

$j_\beta = dN_\beta/dAdEd\Omega dt$ (#/cm^{2}sec Mev sr)

One further convention: the subscript $_\perp$ indicates a flux through a flat surface. E.g., $(I_\beta)_\perp$ means the number of particles of type β crossing a flat unit area per unit time. For an isotropic flux, it is easy to show that

$$(I_\beta)_\perp = \tfrac{1}{2} I_\beta$$

APPENDIX II

THE MONTE CARLO METHOD

A general discussion of Monte Carlo can be found in (Kuo,1966). The basic problem that we wish to solve is this:

> Given a variable x in the interval $(-\infty,\infty)$, how can we select values of x at random, but with probability proportional to a weighting function f(x)?

In order to solve this problem, parameterize x by another random variable t with a domain (0,1) and weighted by a uniform distribution there; i.e., any value of t between 0 and 1 is equally likely.

By the definition of a weighting function,

$$dt = f(x)dx \Big/ \int_{-\infty}^{\infty} f(x)dx \tag{1}$$

Integrating each side up to some fixed limit, we have

$$\int_0^r dt = \int_{-\infty}^{x_o} f(x)dx \Big/ \int_{-\infty}^{\infty} f(x)dx \tag{2}$$

or

$$r = F(x_o) \tag{3}$$

where F is some function of x_o only. But if r is chosen randomly in (0,1), so that each interval Δr is equally probable, then each corresponding interval Δx_o, as defined by the inverse relation

$$x_o = F^{-1}(r) \tag{4}$$

is equally likely. But x_o is just a particular value of x; so if r is chosen by the rule given above, we have a method for finding an x weighted by the probability density f(x).

The problem, as originally stated, then reduces to performing the integration in equation (2), choosing a random number r according to a uniform probability distribution, and inverting equation (3) to find x_o. Most large digital computers have a routine available for generating values of r, which for practical purposes, are uniform on the line segment (0,1). In actuality, these numbers are generated sequentially by a deterministic process and should,strictly speaking, be labelled pseudo-random numbers.

Two examples will elucidate the use of Monte Carlo in our calculations. First suppose a simulated photon is initiated at a depth p_i, and we wish for it to interact at a depth p_f, weighted by the usual exponential attenuation,

$$f(p_f) = e^{-(p_f - p_i)\,\sigma_T/\cos\alpha}$$

Then, in analogy with (2) and (3), let us write

$$r = \frac{\int_{p_i}^{p_f} e^{-(p-p_i)\sigma_T/\cos\alpha}\,dp}{\int_{p_i}^{\infty} e^{-(p-p_i)\sigma_T/\cos\alpha}\,dp}$$

$$r = 1 - e^{-(p_f - p_i)\sigma_T/\cos\alpha}$$

But if r is a random number, weighted by a uniform distribution in(0,1), so is r' = 1-r. Therefore, we can write

$$e^{-(p_f - p_i)\sigma_T/\cos\alpha} = r'$$

or

$$p_f = p_i + (\ln r)\cos\alpha/\sigma$$

Second, suppose we wish to select a zenith angle according to an isotropic distribution, i.e., according to a weighting function $\sin\theta$. Again we can write

$$r = \int_0^\theta \sin\theta' \, d\theta' = 1 - \cos\theta$$

$$\cos\theta = 1 - r = r'$$

or

$$\theta = \cos^{-1} r'.$$

APPENDIX III

Polynomial Coefficients

A. E <1.3 Mev

THE S0(I) - LOW ENERGY

	0	1	2	3	4	5	6	7	8	9
50	IIIII	2.11E+03	2.08E+03	2.05E+03	2.02E+03	2.00E+03	1.98E+03	1.97E+03	1.95E+03	1.94E+03
60	1.93E+03	1.92E+03	1.91E+03	1.90E+03	1.90E+03	1.89E+03	1.88E+03	1.88E+03	1.87E+03	1.87E+03
70	1.87E+03	1.87E+03	1.87E+03	1.86E+03	1.86E+03	1.86E+03	1.86E+03	1.86E+03	1.86E+03	1.86E+03
80	1.86E+03	1.85E+03	1.86E+03	1.86E+03	1.86E+03	1.86E+03	1.86E+03	1.85E+03	1.85E+03	1.86E+03
90	1.86E+03	1.86E+03	1.85E+03	1.85E+03	1.85E+03	1.86E+03	1.86E+03	1.86E+03	1.87E+03	1.87E+03
100	1.87E+03	1.88E+03	1.88E+03	1.89E+03	1.89E+03	1.90E+03	1.90E+03	1.90E+03	1.90E+03	1.90E+03
110	1.90E+03	1.91E+03	1.91E+03	1.91E+03	1.91E+03	1.92E+03	1.92E+03	1.93E+03	1.93E+03	1.93E+03
120	1.93E+03	1.94E+03	1.94E+03	1.94E+03	1.95E+03	1.95E+03	1.95E+03	1.95E+03	1.95E+03	1.95E+03
130	1.95E+03	1.94E+03	1.94E+03	1.93E+03	1.93E+03	1.92E+03	1.91E+03	1.89E+03	1.87E+03	1.85E+03
140	1.82E+03	1.78E+03	1.75E+03	1.70E+03	1.64E+03	1.58E+03	1.51E+03	1.43E+03	1.36E+03	1.28E+03
150	1.20E+03	1.11E+03	1.02E+03	9.34E+02	8.62E+02	8.01E+02	7.45E+02	7.05E+02	6.70E+02	6.38E+02
160	6.10E+02	5.86E+02	5.69E+02	5.53E+02	5.39E+02	5.28E+02	5.17E+02	5.09E+02	5.01E+02	4.96E+02
170	4.91E+02	4.87E+02	4.87E+02	4.88E+02	4.90E+02	4.91E+02	4.92E+02	4.92E+02	4.91E+02	4.85E+02
180	4.75E+02	4.54E+02	4.25E+02	3.81E+02	3.34E+02	2.86E+02	2.46E+02	2.01E+02	1.56E+02	1.29E+02
190	1.11E+02	9.51E+01	7.47E+01	4.60E+01	2.54E+01	2.05E+01	1.71E+01	1.57E+01	-5.64E+00	-2.28E+01
200	-2.45E+01	IIIII	IIIII	IIIII	IIIII	IIIII	IIIII	IIIII	IIIII	IIIII

THE S1(I) - LOW ENERGY

	0	1	2	3	4	5	6	7	8	9
50	IIIII	-2.25E+01	-2.34E+01	-2.41E+01	-2.43E+01	-2.42E+01	-2.42E+01	-2.41E+01	-2.39E+01	-2.38E+01
60	-2.36E+01	-2.33E+01	-2.32E+01	-2.29E+01	-2.26E+01	-2.25E+01	-2.24E+01	-2.23E+01	-2.22E+01	-2.24E+01
70	-2.23E+01	-2.22E+01	-2.21E+01	-2.22E+01	-2.23E+01	-2.23E+01	-2.23E+01	-2.23E+01	-2.22E+01	-2.23E+01
80	-2.23E+01	-2.24E+01	-2.24E+01	-2.23E+01	-2.23E+01	-2.23E+01	-2.23E+01	-2.23E+01	-2.23E+01	-2.23E+01
90	-2.23E+01	-2.22E+01	-2.22E+01	-2.22E+01	-2.22E+01	-2.21E+01	-2.21E+01	-2.20E+01	-2.20E+01	-2.21E+01
100	-2.21E+01	-2.20E+01	-2.19E+01	-2.20E+01	-2.21E+01	-2.21E+01	-2.19E+01	-2.18E+01	-2.17E+01	-2.15E+01
110	-2.14E+01	-2.12E+01	-2.09E+01	-2.09E+01	-2.09E+01	-2.06E+01	-2.05E+01	-2.04E+01	-2.03E+01	-2.01E+01
120	-1.99E+01	-1.96E+01	-1.95E+01	-1.93E+01	-1.91E+01	-1.86E+01	-1.83E+01	-1.79E+01	-1.76E+01	-1.73E+01
130	-1.68E+01	-1.63E+01	-1.58E+01	-1.52E+01	-1.45E+01	-1.39E+01	-1.33E+01	-1.24E+01	-1.17E+01	-1.09E+01
140	-1.04E+01	-9.77E+00	-9.25E+00	-8.95E+00	-8.89E+00	-9.05E+00	-9.41E+00	-9.91E+00	-1.05E+01	-1.12E+01
150	-1.19E+01	-1.08E+01	-9.88E+00	-9.01E+00	-8.30E+00	-7.94E+00	-7.54E+00	-7.39E+00	-7.43E+00	-7.54E+00
160	-7.68E+00	-7.80E+00	-7.93E+00	-8.01E+00	-8.02E+00	-8.12E+00	-8.35E+00	-8.60E+00	-8.78E+00	-8.98E+00
170	-9.20E+00	-9.43E+00	-9.82E+00	-1.02E+01	-1.06E+01	-1.11E+01	-1.15E+01	-1.20E+01	-1.27E+01	-1.35E+01
180	-1.42E+01	-1.45E+01	-1.45E+01	-1.40E+01	-1.34E+01	-1.27E+01	-1.19E+01	-1.10E+01	-9.92E+00	-8.84E+00
190	-7.70E+00	-6.36E+00	-4.87E+00	-3.08E+00	-1.58E+00	-4.76E-01	2.45E-02	-1.21E-01	-1.11E-01	-5.31E-02
200	-1.62E-01	IIIII	IIIII	IIIII	IIIII	IIIII	IIIII	IIIII	IIIII	IIIII

THE S2(I) - LOW ENERGY

	0	1	2	3	4	5	6	7	8	9
50	IIIII	1.31E-01	1.27E-01	1.34E-01	1.51E-01	1.68E-01	1.80E-01	1.85E-01	1.89E-01	1.88E-01
60	1.87E-01	1.86E-01	1.83E-01	1.80E-01	1.77E-01	1.72E-01	1.68E-01	1.64E-01	1.60E-01	1.55E-01
70	1.56E-01	1.58E-01	1.62E-01	1.59E-01	1.55E-01	1.57E-01	1.56E-01	1.54E-01	1.55E-01	1.53E-01
80	1.55E-01	1.55E-01	1.54E-01	1.52E-01	1.54E-01	1.61E-01	1.66E-01	1.71E-01	1.72E-01	1.70E-01
90	1.69E-01	1.72E-01	1.75E-01	1.78E-01	1.81E-01	1.85E-01	1.88E-01	1.89E-01	1.89E-01	1.93E-01
100	1.99E-01	1.97E-01	1.93E-01	1.94E-01	2.01E-01	2.02E-01	1.98E-01	1.93E-01	1.93E-01	1.93E-01
110	1.89E-01	1.85E-01	1.84E-01	1.82E-01	1.79E-01	1.75E-01	1.72E-01	1.73E-01	1.68E-01	1.56E-01
120	1.41E-01	1.31E-01	1.19E-01	1.06E-01	9.27E-02	8.54E-02	7.83E-02	7.52E-02	5.89E-02	4.42E-02
130	3.54E-02	2.73E-02	1.19E-02	-5.99E-03	-2.05E-02	-3.24E-02	-3.63E-02	-3.52E-02	-3.84E-02	-2.76E-02
140	-1.54E-02	-4.54E-03	4.20E-03	1.81E-02	5.01E-02	7.55E-02	9.45E-02	1.15E-01	1.35E-01	1.51E-01
150	1.69E-01	1.64E-01	1.63E-01	1.58E-01	1.54E-01	1.59E-01	1.63E-01	1.60E-01	1.62E-01	1.61E-01
160	1.59E-01	1.60E-01	1.62E-01	1.65E-01	1.69E-01	1.74E-01	1.75E-01	1.75E-01	1.74E-01	1.74E-01
170	1.75E-01	1.78E-01	1.86E-01	1.92E-01	1.98E-01	2.04E-01	2.10E-01	2.17E-01	2.25E-01	2.37E-01
180	2.54E-01	2.78E-01	2.94E-01	3.06E-01	3.17E-01	3.27E-01	3.29E-01	3.33E-01	3.39E-01	3.31E-01
190	3.08E-01	2.72E-01	2.37E-01	1.84E-01	1.32E-01	6.31E-02	1.71E-02	5.87E-03	1.33E-02	1.53E-02
200	2.82E-02	IIIII	IIIII	IIIII	IIIII	IIIII	IIIII	IIIII	IIIII	IIIII

THE S3(I) - LOW ENERGY

	0	1	2	3	4	5	6	7	8	9
50	IIIII	1.53E-03	1.69E-03	1.69E-03	1.57E-03	1.12E-03	7.55E-04	1.41E-04	-4.59E-04	-9.85E-04
60	-1.45E-03	-1.85E-03	-2.09E-03	-2.34E-03	-2.56E-03	-2.69E-03	-2.65E-03	-2.49E-03	-2.36E-03	-2.26E-03
70	-2.21E-03	-2.29E-03	-2.14E-03	-2.19E-03	-2.09E-03	-1.95E-03	-1.85E-03	-1.76E-03	-1.74E-03	-1.72E-03
80	-1.66E-03	-1.53E-03	-1.53E-03	-1.48E-03	-1.44E-03	-1.53E-03	-1.76E-03	-1.96E-03	-2.09E-03	-2.30E-03
90	-2.45E-03	-2.64E-03	-2.75E-03	-2.80E-03	-3.03E-03	-3.05E-03	-3.08E-03	-3.33E-03	-3.50E-03	-3.43E-03
100	-3.36E-03	-3.66E-03	-4.07E-03	-4.19E-03	-4.07E-03	-4.01E-03	-3.98E-03	-3.83E-03	-3.59E-03	-3.38E-03
110	-3.21E-03	-3.14E-03	-2.93E-03	-2.39E-03	-1.96E-03	-1.80E-03	-1.52E-03	-8.67E-04	-1.89E-04	3.98E-04
120	6.73E-04	9.26E-04	1.36E-03	1.88E-03	2.36E-03	2.67E-03	2.96E-03	3.27E-03	3.18E-03	3.20E-03
130	3.48E-03	3.64E-03	3.49E-03	3.34E-03	3.22E-03	3.21E-03	2.96E-03	2.40E-03	1.67E-03	1.39E-03
140	1.28E-03	5.49E-04	-1.53E-04	-6.04E-04	-8.58E-04	-1.33E-03	-1.83E-03	-2.11E-03	-2.33E-03	-2.59E-03
150	-2.88E-03	-3.00E-03	-3.09E-03	-3.09E-03	-3.23E-03	-3.60E-03	-3.97E-03	-3.72E-03	-3.63E-03	-3.43E-03
160	-3.13E-03	-2.95E-03	-3.03E-03	-2.99E-03	-2.98E-03	-3.06E-03	-3.11E-03	-3.12E-03	-3.08E-03	-3.05E-03
170	-3.02E-03	-2.96E-03	-3.11E-03	-3.22E-03	-3.36E-03	-3.56E-03	-3.77E-03	-3.81E-03	-3.96E-03	-4.09E-03
180	-4.37E-03	-4.79E-03	-5.17E-03	-5.89E-03	-6.93E-03	-8.08E-03	-8.66E-03	-9.41E-03	-1.01E-02	-9.80E-03
190	-9.00E-03	-8.15E-03	-7.61E-03	-6.58E-03	-5.24E-03	-2.83E-03	-9.86E-04	-1.13E-04	3.73E-05	8.64E-05
200	-1.23E-03	IIIII	IIIII	IIIII	IIIII	IIIII	IIIII	IIIII	IIIII	IIIII

THE S4(I) - LOW ENERGY

	0	1	2	3	4	5	6	7	8	9
50	IIIII	7.09E-05	7.62E-05	6.99E-05	5.53E-05	3.54E-05	2.87E-05	2.42E-05	2.13E-05	3.23E-05
60	4.34E-05	5.54E-05	7.15E-05	7.40E-05	7.57E-05	8.88E-05	1.07E-04	1.23E-04	1.29E-04	1.33E-04
70	1.32E-04	1.24E-04	1.29E-04	1.31E-04	1.32E-04	1.25E-04	1.23E-04	1.26E-04	1.22E-04	1.19E-04
80	1.14E-04	1.13E-04	1.11E-04	1.16E-04	1.25E-04	1.20E-04	1.10E-04	1.03E-04	1.03E-04	1.03E-04
90	1.03E-04	1.01E-04	1.03E-04	1.12E-04	1.11E-04	1.15E-04	1.18E-04	1.13E-04	1.13E-04	1.15E-04
100	1.15E-04	1.14E-04	1.07E-04	9.81E-05	9.46E-05	1.01E-04	8.92E-05	7.76E-05	6.69E-05	5.36E-05
110	4.18E-05	2.87E-05	9.86E-06	1.01E-05	1.66E-06	-1.62E-05	-3.24E-05	-4.96E-05	-5.64E-05	-5.12E-05
120	-5.95E-05	-7.94E-05	-8.96E-05	-9.15E-05	-8.95E-05	-1.05E-04	-1.22E-04	-1.30E-04	-1.30E-04	-1.22E-04
130	-1.12E-04	-1.02E-04	-8.78E-05	-6.37E-05	-3.97E-05	-1.88E-05	-8.15E-06	8.59E-07	5.24E-06	1.87E-05
140	3.49E-05	2.34E-05	3.00E-05	4.66E-05	3.49E-05	3.20E-05	3.33E-05	3.92E-05	4.27E-05	4.82E-05
150	5.50E-05	6.44E-05	6.49E-05	6.90E-05	6.64E-05	6.60E-05	7.03E-05	5.76E-05	5.19E-05	5.12E-05
160	4.91E-05	4.83E-05	4.88E-05	5.16E-05	5.07E-05	4.89E-05	4.23E-05	3.79E-05	3.99E-05	4.19E-05
170	4.18E-05	3.96E-05	4.31E-05	4.70E-05	5.18E-05	5.67E-05	6.10E-05	6.60E-05	6.55E-05	6.79E-05
180	7.67E-05	8.94E-05	9.20E-05	9.43E-05	9.86E-05	1.11E-04	1.21E-04	1.28E-04	1.44E-04	1.37E-04
190	1.28E-04	1.31E-04	1.34E-04	1.13E-04	7.99E-05	6.26E-05	5.13E-05	5.90E-05	5.20E-05	4.82E-05
200	7.62E-05	IIIII	IIIII	IIIII	IIIII	IIIII	IIIII	IIIII	IIIII	IIIII

THE S5(I) - LOW ENERGY

	0	1	2	3	4	5	6	7	8	9
50	IIIII	-1.54E-06	-1.92E-06	-2.27E-06	-2.94E-06	-2.89E-06	-2.62E-06	-2.62E-06	-2.72E-06	-2.55E-06
60	-2.63E-06	-2.81E-06	-2.87E-06	-3.67E-06	-4.44E-06	-4.70E-06	-5.09E-06	-5.64E-06	-6.16E-06	-6.29E-06
70	-6.30E-06	-6.36E-06	-5.82E-06	-5.30E-06	-5.38E-06	-5.85E-06	-5.73E-06	-5.33E-06	-5.35E-06	-5.26E-06
80	-5.14E-06	-5.12E-06	-5.08E-06	-5.18E-06	-5.13E-06	-4.82E-06	-4.34E-06	-3.81E-06	-3.70E-06	-3.67E-06
90	-3.69E-06	-3.54E-06	-3.21E-06	-2.63E-06	-2.39E-06	-2.32E-06	-2.17E-06	-2.05E-06	-1.61E-06	-1.13E-06
100	-8.30E-07	-3.00E-07	4.33E-07	6.08E-07	1.08E-06	1.66E-06	1.96E-06	2.84E-06	3.78E-06	4.28E-06
110	4.91E-06	5.85E-06	6.21E-06	6.98E-06	7.40E-06	7.41E-06	7.37E-06	7.16E-06	7.07E-06	7.65E-06
120	7.95E-06	7.88E-06	7.72E-06	7.32E-06	7.00E-06	6.23E-06	5.81E-06	5.64E-06	5.63E-06	5.80E-06
130	5.17E-06	4.09E-06	3.72E-06	3.16E-06	2.28E-06	1.34E-06	1.16E-06	1.31E-06	1.20E-06	1.09E-06
140	7.70E-07	-1.52E-07	-1.02E-07	5.92E-07	6.89E-07	8.85E-07	1.27E-06	1.38E-06	1.19E-06	9.14E-07
150	7.68E-07	3.97E-07	7.81E-07	7.34E-07	4.78E-07	6.47E-07	1.04E-06	1.14E-06	8.63E-07	1.93E-07
160	-2.08E-07	-3.27E-07	-1.84E-07	-5.59E-08	-1.69E-07	-2.12E-07	-2.76E-07	-3.39E-07	-6.41E-07	-9.65E-07
170	-1.05E-06	-1.01E-06	-1.03E-06	-1.21E-06	-1.35E-06	-1.39E-06	-1.37E-06	-1.67E-06	-1.80E-06	-1.83E-06
180	-1.67E-06	-1.58E-06	-1.67E-06	-3.36E-07	9.70E-07	1.89E-06	2.40E-06	3.33E-06	3.91E-06	3.42E-06
190	2.56E-06	1.67E-06	1.27E-06	2.06E-06	4.03E-06	2.55E-06	-5.30E-07	-4.07E-06	-5.26E-06	-6.27E-06
200	-7.20E-06	IIIII	IIIII	IIIII	IIIII	IIIII	IIIII	IIIII	IIIII	IIIII

ALPHA1= 71.27 ALPHA2= 86.28 ALPHA3= 81.55 ALPHA4= 76.57 ALPHA5= 81.61
BETA1= 780.9 BETA2= 713.4 BETA3= 578.9 BETA4= 562.2

B. E > 1.3 Mev

THE S0(I) - HIGH ENERGY

	0	1	2	3	4	5	6	7	8	9
50	IIIII	7.65E+02	7.42E+02	7.22E+02	7.07E+02	6.97E+02	6.87E+02	6.84E+02	6.80E+02	6.79E+02
60	6.77E+02	6.79E+02	6.73E+02	6.67E+02	6.66E+02	6.58E+02	6.52E+02	6.42E+02	6.42E+02	6.41E+02
70	6.36E+02	6.35E+02	6.35E+02	6.35E+02	6.34E+02	6.34E+02	6.32E+02	6.31E+02	6.27E+02	6.22E+02
80	6.26E+02	6.26E+02	6.30E+02	6.25E+02	6.28E+02	6.23E+02	6.26E+02	6.24E+02	6.23E+02	6.25E+02
90	6.24E+02	6.30E+02	6.32E+02	6.38E+02	6.42E+02	6.48E+02	6.65E+02	6.88E+02	7.07E+02	7.39E+02
100	7.45E+02	7.27E+02	7.06E+02	6.95E+02	6.89E+02	6.83E+02	6.79E+02	6.76E+02	6.76E+02	6.70E+02
110	6.65E+02	6.66E+02	6.69E+02	6.74E+02	6.75E+02	6.66E+02	6.65E+02	6.68E+02	6.72E+02	6.73E+02
120	6.73E+02	6.75E+02	6.79E+02	6.83E+02	6.84E+02	6.81E+02	6.83E+02	6.86E+02	6.92E+02	6.94E+02
130	6.98E+02	7.00E+02	7.06E+02	7.07E+02	7.09E+02	7.15E+02	7.14E+02	7.18E+02	7.24E+02	7.21E+02
140	7.26E+02	7.39E+02	7.47E+02	7.68E+02	7.87E+02	8.13E+02	8.47E+02	8.84E+02	9.25E+02	9.62E+02
150	1.00E+03	1.02E+03	1.03E+03	1.04E+03	1.04E+03	1.04E+03	1.03E+03	1.03E+03	1.02E+03	1.01E+03
160	1.00E+03	9.86E+02	9.75E+02	9.64E+02	9.64E+02	9.69E+02	9.74E+02	9.76E+02	9.77E+02	9.71E+02
170	9.67E+02	9.72E+02	9.75E+02	9.69E+02	9.71E+02	9.67E+02	9.71E+02	9.70E+02	9.77E+02	9.88E+02
180	9.91E+02	1.00E+03	1.01E+03	1.01E+03	1.01E+03	1.02E+03	1.02E+03	1.01E+03	9.94E+02	9.89E+02
190	9.74E+02	9.60E+02	9.33E+02	9.08E+02	8.76E+02	8.37E+02	7.89E+02	7.48E+02	7.09E+02	6.61E+02
200	6.28E+02	6.01E+02	5.66E+02	5.38E+02	5.08E+02	4.78E+02	4.50E+02	4.20E+02	3.92E+02	3.66E+02
210	3.41E+02	3.20E+02	3.03E+02	2.83E+02	2.64E+02	2.48E+02	2.30E+02	2.11E+02	1.96E+02	1.79E+02
220	1.66E+02	1.56E+02	1.45E+02	1.32E+02	1.16E+02	9.83E+01	8.12E+01	6.27E+01	4.72E+01	2.67E+01
230	1.10E+01	IIIII	IIIII	IIIII	IIIII	IIIII	IIIII	IIIII	IIIII	IIIII

THE S1(I) - HIGH ENERGY

	0	1	2	3	4	5	6	7	8	9
50	IIIII	-6.28E+00	-6.20E+00	-6.02E+00	-5.87E+00	-5.76E+00	-5.76E+00	-5.69E+00	-5.64E+00	-5.60E+00
60	-5.56E+00	-5.58E+00	-5.50E+00	-5.48E+00	-5.48E+00	-5.31E+00	-5.17E+00	-4.95E+00	-4.90E+00	-4.89E+00
70	-4.82E+00	-4.79E+00	-4.76E+00	-4.70E+00	-4.67E+00	-4.64E+00	-4.63E+00	-4.57E+00	-4.49E+00	-4.43E+00
80	-4.48E+00	-4.45E+00	-4.43E+00	-4.30E+00	-4.30E+00	-4.23E+00	-4.26E+00	-4.24E+00	-4.23E+00	-4.20E+00
90	-4.14E+00	-4.14E+00	-4.15E+00	-4.16E+00	-4.12E+00	-4.03E+00	-3.98E+00	-3.78E+00	-3.32E+00	-2.23E+00
100	-1.83E+00	-1.74E+00	-1.58E+00	-1.75E+00	-1.89E+00	-1.98E+00	-2.09E+00	-2.25E+00	-2.32E+00	-2.55E+00
110	-2.49E+00	-2.46E+00	-2.55E+00	-2.68E+00	-2.65E+00	-2.46E+00	-2.50E+00	-2.53E+00	-2.49E+00	-2.52E+00
120	-2.46E+00	-2.46E+00	-2.44E+00	-2.50E+00	-2.52E+00	-2.46E+00	-2.38E+00	-2.40E+00	-2.45E+00	-2.48E+00
130	-2.57E+00	-2.61E+00	-2.68E+00	-2.67E+00	-2.67E+00	-2.71E+00	-2.82E+00	-2.83E+00	-2.88E+00	-2.78E+00
140	-2.66E+00	-2.53E+00	-2.38E+00	-2.31E+00	-1.94E+00	-1.71E+00	-1.36E+00	-9.23E-01	-5.91E-01	-3.76E-01
150	-1.86E-01	-7.29E-02	7.85E-02	2.35E-01	4.35E-01	3.91E-01	3.60E-01	1.93E-01	9.20E-02	-5.41E-02
160	-2.12E-01	-4.81E-01	-8.84E-01	-1.16E+00	-1.58E+00	-1.86E+00	-2.15E+00	-2.26E+00	-2.36E+00	-2.58E+00
170	-2.63E+00	-2.75E+00	-2.91E+00	-2.93E+00	-3.19E+00	-3.31E+00	-3.50E+00	-3.54E+00	-3.67E+00	-3.80E+00
180	-3.85E+00	-4.11E+00	-4.15E+00	-4.25E+00	-4.38E+00	-4.61E+00	-4.73E+00	-4.76E+00	-4.70E+00	-4.74E+00
190	-4.74E+00	-4.64E+00	-4.45E+00	-4.36E+00	-4.09E+00	-3.81E+00	-3.34E+00	-2.90E+00	-2.72E+00	-2.50E+00
200	-2.20E+00	-2.04E+00	-1.78E+00	-1.65E+00	-1.52E+00	-1.37E+00	-1.24E+00	-1.14E+00	-1.01E+00	-9.78E-01
210	-9.03E-01	-8.32E-01	-7.73E-01	-7.21E-01	-6.87E-01	-6.52E-01	-5.65E-01	-5.55E-01	-5.79E-01	-5.53E-01
220	-4.79E-01	-4.22E-01	-3.23E-01	-2.37E-01	-1.51E-01	-5.47E-02	2.20E-01	5.31E-01	7.73E-01	9.78E-01
230	1.17E+00	IIIII	IIIII	IIIII	IIIII	IIIII	IIIII	IIIII	IIIII	IIIII

THE S2(I) - HIGH ENERGY

	0	1	2	3	4	5	6	7	8	9
50	IIIII	3.32E-02	4.22E-02	4.64E-02	4.83E-02	4.83E-02	4.58E-02	4.43E-02	4.41E-02	4.27E-02
60	4.12E-02	4.15E-02	4.00E-02	4.02E-02	3.95E-02	3.57E-02	3.08E-02	2.55E-02	2.40E-02	2.44E-02
70	2.44E-02	2.46E-02	2.47E-02	2.42E-02	2.46E-02	2.41E-02	2.57E-02	2.44E-02	2.53E-02	2.55E-02
80	2.65E-02	2.60E-02	2.48E-02	2.37E-02	2.39E-02	2.62E-02	2.75E-02	2.91E-02	2.94E-02	2.83E-02
90	2.60E-02	2.50E-02	2.77E-02	2.81E-02	2.69E-02	2.44E-02	2.00E-02	1.08E-02	1.35E-03	9.89E-03
100	1.75E-02	2.45E-02	2.56E-02	3.26E-02	3.50E-02	3.32E-02	3.65E-02	3.38E-02	3.27E-02	2.87E-02
110	2.25E-02	2.36E-02	2.22E-02	2.08E-02	2.03E-02	1.87E-02	1.95E-02	2.15E-02	2.01E-02	2.06E-02
120	1.61E-02	1.66E-02	1.56E-02	1.76E-02	1.79E-02	1.90E-02	1.72E-02	1.56E-02	1.42E-02	1.34E-02
130	1.61E-02	1.67E-02	1.60E-02	1.46E-02	1.36E-02	1.50E-02	1.32E-02	1.48E-02	1.49E-02	1.31E-02
140	1.45E-02	1.51E-02	1.59E-02	1.15E-02	1.67E-02	1.57E-02	1.37E-02	1.54E-02	1.03E-02	4.92E-03
150	-1.31E-03	-1.48E-03	-1.93E-03	-1.04E-03	3.27E-04	1.83E-03	6.32E-05	2.52E-03	1.46E-04	3.76E-03
160	6.08E-03	7.83E-03	1.34E-02	1.27E-02	1.51E-02	1.75E-02	2.37E-02	2.71E-02	2.51E-02	2.42E-02
170	2.32E-02	2.35E-02	2.30E-02	1.96E-02	1.72E-02	1.25E-02	1.17E-02	9.27E-03	1.03E-02	8.74E-03
180	7.77E-03	1.18E-02	1.31E-02	1.43E-02	1.64E-02	2.23E-02	2.47E-02	2.72E-02	2.78E-02	2.58E-02
190	2.88E-02	2.95E-02	2.85E-02	2.68E-02	2.23E-02	2.04E-02	1.54E-02	1.13E-02	9.31E-03	6.78E-03
200	4.92E-03	7.91E-03	6.55E-03	6.20E-03	4.84E-03	3.09E-03	9.76E-04	1.75E-03	-4.81E-05	6.92E-04
210	1.11E-03	2.25E-03	2.23E-03	2.50E-03	2.44E-03	3.21E-03	4.71E-03	7.56E-03	8.62E-03	1.11E-02
220	1.24E-02	1.30E-02	1.45E-02	1.72E-02	1.94E-02	2.26E-02	2.71E-02	3.21E-02	3.40E-02	3.67E-02
230	3.83E-02	IIIII	IIIII	IIIII	IIIII	IIIII	IIIII	IIIII	IIIII	IIIII

THE S3(I) - HIGH ENERGY

	0	1	2	3	4	5	6	7	8	9
50	IIIII	-1.13E-03	-1.27E-03	-1.42E-03	-1.52E-03	-1.53E-03	-1.55E-03	-1.50E-03	-1.52E-03	-1.50E-03
60	-1.47E-03	-1.46E-03	-1.39E-03	-1.39E-03	-1.31E-03	-1.17E-03	-9.15E-04	-7.62E-04	-8.22E-04	-8.17E-04
70	-7.82E-04	-7.58E-04	-7.90E-04	-8.24E-04	-7.93E-04	-7.53E-04	-7.43E-04	-7.07E-04	-8.29E-04	-7.88E-04
80	-7.68E-04	-7.71E-04	-7.58E-04	-8.05E-04	-7.98E-04	-8.88E-04	-8.50E-04	-8.79E-04	-8.39E-04	-8.83E-04
90	-7.81E-04	-7.88E-04	-7.99E-04	-7.24E-04	-6.25E-04	-5.08E-04	-4.62E-04	-5.06E-04	-5.93E-04	-6.86E-04
100	-6.92E-04	-8.49E-04	-6.28E-04	-4.50E-04	-4.00E-04	-3.08E-04	-2.74E-04	-2.82E-04	-2.91E-04	-3.39E-04
110	-3.39E-04	-3.07E-04	-3.62E-04	-3.89E-04	-3.73E-04	-3.40E-04	-3.88E-04	-4.68E-04	-4.19E-04	-4.51E-04
120	-2.58E-04	-2.44E-04	-2.23E-04	-3.06E-04	-3.33E-04	-4.02E-04	-3.40E-04	-2.59E-04	-2.26E-04	-1.16E-04
130	-1.28E-04	-1.23E-04	-6.56E-05	-6.01E-05	-3.62E-05	-3.89E-06	8.20E-06	-2.54E-06	-3.37E-05	-1.18E-04
140	-5.37E-05	-1.31E-04	-2.32E-04	-1.11E-04	-6.34E-05	-8.08E-05	-8.74E-05	-4.13E-05	4.76E-06	1.03E-04
150	1.23E-04	1.05E-04	-9.70E-06	-8.85E-05	-2.18E-04	-1.03E-04	-2.57E-04	-2.39E-04	-2.19E-04	-1.72E-04
160	-1.08E-04	-1.33E-04	-1.95E-04	-2.11E-04	-2.82E-04	-4.78E-04	-6.43E-04	-6.14E-04	-6.97E-04	-6.82E-04
170	-7.23E-04	-7.60E-04	-7.31E-04	-7.11E-04	-7.63E-04	-8.05E-04	-8.04E-04	-8.08E-04	-7.38E-04	-6.34E-04
180	-6.75E-04	-5.83E-04	-5.87E-04	-5.46E-04	-5.57E-04	-4.32E-04	-3.29E-04	-3.81E-04	-3.57E-04	-4.06E-04
190	-4.80E-04	-3.73E-04	-1.82E-04	-1.75E-04	-1.55E-04	-1.12E-04	1.13E-04	1.26E-04	9.37E-05	1.99E-04
200	3.11E-04	3.20E-04	2.52E-04	3.04E-04	3.35E-04	3.23E-04	3.23E-04	3.51E-04	3.65E-04	4.22E-04
210	4.13E-04	4.38E-04	4.31E-04	3.81E-04	3.46E-04	3.56E-04	3.31E-04	3.53E-04	4.30E-04	4.91E-04
220	5.16E-04	5.49E-04	5.29E-04	5.07E-04	4.94E-04	4.82E-04	4.60E-04	4.83E-04	4.95E-04	4.91E-04
230	5.56E-04	IIIII	IIIII	IIIII	IIIII	IIIII	IIIII	IIIII	IIIII	IIIII

ALPHA1= 176.5 ALPHA2= 213.6 ALPHA3= 191.8 BETA1=2204.3 BETA2=1469.0

REFERENCES

Arnold, J. R., A. E. Metzger, E. C. Anderson, and M. A. Van Dilla, J. Geophys. Res. 67, 4878, 1962.

Ascher, M., and G. E. Forsythe, J. Assoc. for Comp. Mach., 5 9, 1958.

Bethe, H. A., and J. Ashkin, Experimental Nuclear Physics I, Wiley Inc., N. Y., 166, E. Segre, ed., 1953.

Bethe, H. A., and W. Heitler, Proc. Roy. Soc. (London), A146, 83, 1934.

Bradt, H., S. Rappaport, W. Mayer, R. E. Warner, B. MacFarlane, and J. Kristian, Nature 222, 728, 1969.

Brini, D., V. Ciriegi, F. Fuligni and E. Moretti, J. Geophys. Res., 72, 903, 1967.

Brini, D., Private communication, 1970.

Burbidge, G. R., E. M. Burbidge, W. A. Fowler, and F. Hoyle, Rev. Mod. Phys., 29, 547, 1957.

Charakhch'ian, A. N., and T. N. Charakhch'ian, Soviet Physics JETP, 35, 761 1959.

Chupp, E. L., D. J. Forrest, A. A. Sarkady, and P. J. Lavakare, Low Energy Gamma Radiation in the Atmosphere During Active and Quiet Periods on the Sun, Univ. N. H. Rep., 1969.

Chupp, E. E., H. P. Gilman, and A. A. Sarkady, The .51 Mev Gamma Ray Flux and the Energy Loss Spectrum in Cs I (T1) at 4 gms/cm^2, Univers. N. H. Rep., 1966.

Clayton, D. D., and W. L. Craddock, Astrophys. J., 142, 189, 1965.

Clayton, D. D., S. A. Colgate, and G. J. Fishman, Astrophys. J., 155, 75, 1969.

Clayton, D. D., and J. Silk, Astrophys. J., 158, L43, 1969.

Davisson, C. M., Alpha-, Beta-, and Gamma-Ray Spectroscopy I, North-Holland Pub. Co., Amsterdam, 827, K. Siegbahn, ed.,

Dolan, J. F., and G. G. Fazio, Rev. of Geophys., 3, 319, 1965.

Evans, R. D., The Atomic Nucleus, McGraw-Hill Book Co., N. Y., 1955.

Fazio, G. G., Ann. Rev. Astron. Astrophys., 5, 481, 1967.

Fishman, G. H., F. R. Harnden Jr., and R. C. Haymes, Astrophys. J., L107, 1969.

Fowler, W. A., J. L. Greenstein, and F. Hoyle, Geophys. J., Roy. Ast. Soc., 6, 148, 1962

Fritz, G., R. C. Henry, J. F. Meekins, T. A. Chubb, and H. Friedman, Science, 164, 709, 1969.

Ginsburg, V. L., and S. I. Syrovatskii, a. The Origin of Cosmic Rays, Macmillan Co., N.Y., 1964; b. Soviet Phys. Usp. 84, 201, 1964.

Gould, R. J., and G. R. Burbidge, Ann. Astrophys. 28,171, 1965.

Greisen, K., Brandeis Summer Lecture Series, 1968.

Guernsey, J. B., and D. A. Lind, Fast Neutron Physics II, Wiley-Interscience, N. Y., 1483, J. B. Marion and J. L. Fowler, Ed., 1963.

Hall, H. E., and T. W. Bonner, Nuc. Phys., 14, 295, 1959.

Hayakawa, S., Cosmic Ray Physics,Wiley-Interscience, N. Y., 1969.

Haymes, R. C., J. Geophys. Res.,69, 841, 1964.

Haymes, R. C., D. V. Ellis, G. J. Fishman, S. W. Glenn, and J. D. Kurfess, Astrophys. J., 151, L9, 1968.

Heath, R. L., Scintillation Spectrometry, Gamma Ray Spectrum Catalogue I, AEC Rep., IDO-16880, 1964.

Heath, R. L., R. G. Helmer, L. A. Schmittroth, and G. A. Cazier, The Calculation of Gamma Ray Shapes for NaI Scintillation Spectrometers, AEC Rep., IDO-17017, 1965.

Hughes, D. J., and R. B. Schwartz, Neutron Cross Sections, B. N. L. Rep. BNL-325, Suppl. No. 2, 1964.

Israel, M. H., J. Geophys. Res., 74, 4701, 1969.

Kouts, H. J., and L. Yuan, Phys. Rev., 86, 128, 1952.

Kuo, S. S., Numerical Methods and Computers, Addison-Wesley, Reading, Mass., 1965.

Kuzhevskii, B. M., Soviet Astron., 12, 595, 1969.

Lowder, W. M., NASA Rep., N69-41043, 1969.

Metzger, A. E., E. C. Anderson, M. A. Van Dilla, and J. R. Arnold, Nature, 204, 766, 1964.

Muehlhause, C. O., Phys. Rev., 79, 277, 1950.

Perola, G. C., and L. Scarsi, Nuovo Cimento, 46, 718, 1966.

Peterson, L. E., Private communication, 1969.

Rocchia, R., Rayonnement Gamma dans L'Espace et dans L'Atmosphere, Ph. D. Thesis, Univers. of Paris, 1966.

Sandstrom, A. E., Cosmic Ray Physics, North-Holland Pub. Co., Amsterdam, 1965.

Sartori, L., and P. Morrison, Astrophys. J., 150, 385, 1967.

Savedoff, M. P., Nuovo Cimento, 13, 12, 1959.

Stecker, F. W., Production of Cosmic Gamma Rays in Cosmic-Ray Collisions III, Smithsonian Astrophys. Obs. Spec. Rep. No. 260, 1967.

Trombka, R., Private communication, 1970.

Verma, S. D., J. Geophys. Res., 72, 915, 1967.

Vette, J., J. L. Matteson, D. Gruber, and L. E. Peterson, Proceeding of IAU Symposium No. 37 on Non-Solar Gamma and X-Ray Astronomy, Rome, 1969.

Zerby, C. D., Methods in Comp. Phys., 1, 89, 1963.